Supplemental Material
Foam-like Properties in Networks of Bundled Semiflexible Polymers

Lukas P. Weise, Tobias A. Kampmann, and Jan Kierfeld*
Physics Department, TU Dortmund University, 44221 Dortmund, Germany
(Dated: January 6, 2026)

CONTENTS

* Contact author: jan.kierfeld@tu-dortmund.de

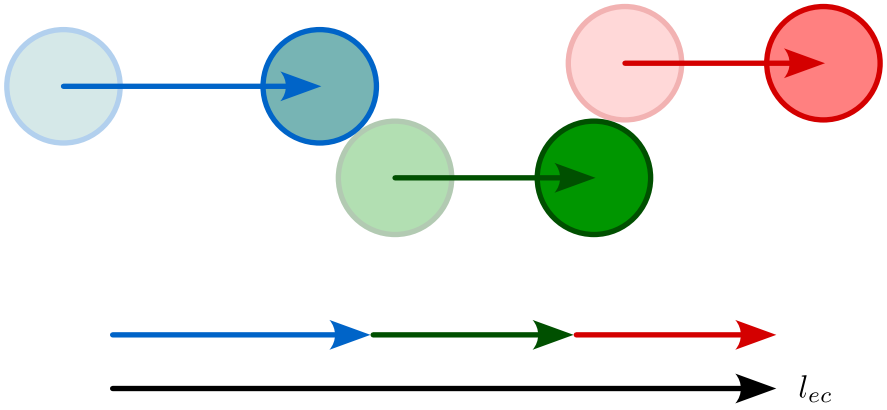

FIG. S1. Displacements of three hard spheres generated by the ECMC algorithm. The blue sphere is displaced until there is a collision with some other sphere. Now the collision partner (green) is moved along the same direction to the collision point with the red sphere, which (in this example) is displaced until l_{ec} is reached. The direction $\mathbf{d}_{ec}$ defines the x-axis in this sketch; in general $\mathbf{d}_{ec}$ does not need to be aligned with any coordinate axis of the simulation volume.

I. OUTLINE OF THE EVENT-CHAIN MONTE CARLO ALGORITHM

In this section we present a phenomenological description of the event-chain Monte Carlo (ECMC) algorithm used in some of the simulations. We aim to provide an intuitive understanding of the basic principles of ECMC. A rigorous treatment of the mathematical foundations can be found in the reviews [1, 2].

We begin our outline of the ECMC algorithm by considering a system of hard spheres of diameter σ. We generate samples by performing rejection-free cluster moves, so-called *event-chains* (ECs), which displace many spheres in one EC move. The number of participating particles can be controlled by the *EC length* l_{ec}, which is the total displacement length of all spheres participating in an EC. For each EC move, we choose a random displacement direction $\mathbf{d}_{ec}$ on the unit sphere and select a random sphere as initial *active particle*. Next, the selected sphere is displaced along $\mathbf{d}_{ec}$ until it either collides with another sphere or the total displacement length has reached l_{ec}. Upon a collision, there is no rejection but the pseudo-momentum is transferred to the collision partner and the collision partner becomes the active sphere in a so-called *lifting event*. Now, the new active sphere is displaced in $\mathbf{d}_{ec}$-direction until there is another collision and lifting event or the total displacement reaches l_{ec}. This process is shown in Fig. S1 for three hard spheres.

Once the total displacement amounts to l_{ec}, a new direction $\mathbf{d}_{ec}$ and active particle are chosen and a new EC is started. Compared to conventional MC, the ECMC converts all rejection events into lifting events and, therefore, is rejection-free. This property is particularly advantageous for simulations of (locally) densely packed spheres where traditional MC schemes often cannot generate acceptable moves efficiently.

The generalization to continuous pair potentials like the Lennard-Jones potential builds upon the hard sphere case by assigning an effective hard sphere diameter σ_{eff} to the collision partner. To this end, an exponentially distributed random number is generated specifying the usable uphill energy $\beta\Delta E^*$ (energies in units of $k_BT = \beta^{-1}$). A lifting event is triggered, when the potential between the two particles has increased by ΔE^* (see Fig. S2).

Similar to local MC, we do not take any attractive parts (i.e. energy downhill) of the pair potential into account for the computation of σ_{eff} because energy decreasing displacements cannot create rejections that are converted into lifting events. The same logic is valid for non-central collisions of particles albeit the energy landscape will generally become more complicated than the example shown in Fig. S2.

Thus far we have only discussed interactions involving two particles, i.e. the lifting is deterministic. To simulate systems like the bundled polymer networks, we also have to consider one-particle interactions (collisions with a hard wall imposed by our boundary conditions in z-direction) and three-particle interactions (bending stiffness). One-particle interactions are particularly simple: instead of lifting to a different particle, the direction is reflected $\mathbf{d}_{ec} \to \mathbf{d}_{ec} - 2(\mathbf{d}_{ec} \cdot \mathbf{n})\mathbf{n}$ with respect to the surface normal $\mathbf{n}$ if the particle collides with the hard wall (a similar logic would apply to a soft wall potential, although this case is not relevant for our study). A reflection of the displacement direction at the wall is the correct treatment for the ECMC algorithm as has been shown in Ref. [3].

The lifting rules for three-particle interactions (or, in principle, any number of particles) revolve around finding the correct lifting probabilities λ_{ij} for lifting from the event-causing particle i to one of the two (or more) interacting particles j. As an example, we consider the case of a bending event caused by the red sphere in Fig. S3.

The lifting probabilities λ_{ij} are found to depend crucially on the directional derivatives of the respective interaction

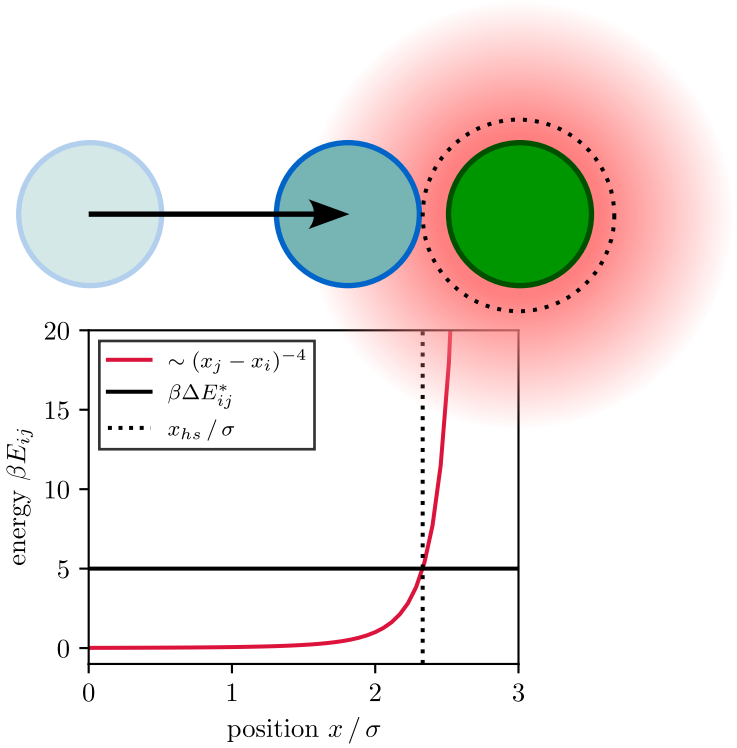

FIG. S2. Lifting for a generic repulsive and continuous potential (red graph and corona). The active particle (blue) is displaced from $x_b = 0$ and "collides" with the green particle located at $x_g = 3\,\sigma$. The effective hard sphere diameter $\sigma_{eff} = 2|x_{hs} - x_g|$ (dotted line) is determined by the intersection of the usable uphill energy ΔE^* and the pair potential. Again, the direction $\mathbf{d}_{ec}$ defines the x-axis.

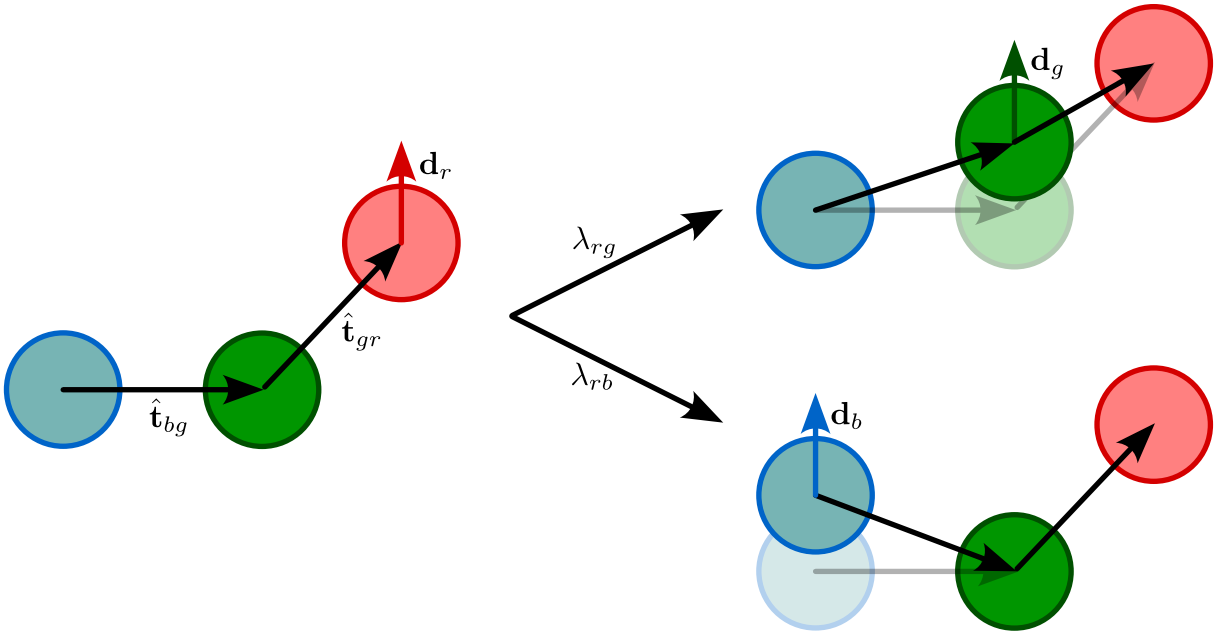

FIG. S3. Lifting for a three particle bending interaction with energy $\propto (1 - \hat{\mathbf{t}}_{bg} \cdot \hat{\mathbf{t}}_{gr})$. As an example, we consider a rejection caused by the displacement of the red sphere (left). The lifting can transfer the pseudo-momentum either to the green or the blue sphere. However, the bending interaction favours a straight conformation and, in this case, only moving the green sphere upwards reduces the energy and we have $\lambda_{rg} = 1$, $\lambda_{rb} = 0$.

energy with respect to particle displacement along $\mathbf{d}_{ec}$. Visually speaking, lifting to e.g. the green sphere becomes more probable for a larger energy decrease effected by the displacement of the green sphere along $\mathbf{d}_{ec}$. The situation shown in Fig. S3 is particularly simple; for the given direction only a move of the green sphere reduces the energy.

To conclude our brief outline of the algorithm, we want to emphasize the local nature of the particle displacements generated by ECMC. During one EC, a particle is moved by l_{ec} at most (with $l_{ec} = \sigma$ in our simulations). Although the ECMC dynamics is not a physical dynamics by definition, these local displacements give rise to an ECMC dynamics which reproduces different diffusive regimes observed in MD simulations of polymer melts [4]. Given that the ECMC algorithm was successfully applied to polymer melts, we simulate the polymer systems presented in this study with ECMC and find very similar coarsening rates for the polymer systems with LJ interaction simulated with MD and EC (see main text Fig. 2f). The horizontal offset therein between ECMC and MD simulation time depends on the definition of the term "sweep". By convention, a single sweep corresponds to starting (on average) one EC per particle. However, one EC will typically displace many particles by small amounts along its propagation through the volume. The number of displaced particles can be estimated as $n_{disp} \approx l_{ec}/d_{mfp}n_{eq}$ with the mean rejection length (or mean free path) d_{mfp} and the average number of times a particle is displaced by one EC n_{eq} (e.g. due to attractive interactions). A MD time step Δt, on the other hand, displaces all n_{part} particles by a small amount. We estimate the average number of event chains necessary to move all particles as $n_{ec} \approx n_{part}/n_{disp} \approx n_{part}d_{mfp}n_{eq}/l_{ec}$, which roughly corresponds to one MD time step. The mapping between a sweep and Δt will therefore scale as $1\,\mathrm{sw} \sim (n_{part}/n_{ec})\Delta t \approx (l_{ec}/d_{mfp}n_{eq})\,\Delta t$. We do not expect the time mapping to change significantly during the simulations as densely packed bundle form quickly after the initialization and, therefore, the mean particle displacement per event chain $d_{mfp}n_{eq}$ does not change significantly. Considering the stochastic nature of the EC displacement directions $\mathbf{d}_{ec}$ and the inability to take inertia into account, this scaling will be a valid approximation only for systems with strong damping and strong influence of thermal fluctuations. Both of these criteria apply to our simulations with an energy scale of the attraction $\sim k_BT$ and the linear displacement of polymers observed in SM Sec. IX.

II. PARAMETER REQUIREMENTS FOR NETWORK FORMATION

The system of mutually attractive semiflexible polymers forms networks of bundles over a wide range of parameters. Nevertheless there are a few requirements on the parameters of the simulated system, to obtain a continuous, volume spanning network of polymer bundles. Clearly, there must be a sufficiently high polymer concentration and the attractive strength must exceed the critical potential strength for bundling [5], so that polymers come into contact and form stable bundles. As a consequence of the polymers' mutual and self attraction, polymers must provide a certain degree of stiffness to prevent coiling and collapse. Less obvious conditions apply to the individual polymer length, i.e., number of beads and the range of the attractive potential. If the polymer length is smaller than the persistence length, the polymers exhibit a rod-like behaviour and the isotropically initialized system evolves to many short, but unconnected, bundles and eventually these bundles merge into one large cluster. The attractive interactions must not be very short ranged $d \leq 1.2\,\sigma$. In the case of such short-ranged attractive potentials, the polymers form few separate bundles of larger diameter that, however, do not assemble to a meshed network. These conditions are in qualitative agreement with observations in Ref. [6–8].

We choose the simulation parameters to produce networks of bundles reliably while keeping the computational effort reasonable. A combination of 2800 polymers with 100 beads each in a simulation volume of $800\,\sigma \times 800\,\sigma \times 10\,\sigma$ is found to be a good choice to form volume-spanning networks. The observed network structure is not very sensitive to the polymer length provided that the parameters are in the regime of the bundle networks. Similar findings are reported in other simulation studies of mutually attractive semiflexible polymers [6, 9].

The *bending stiffness* is set to $\kappa = 30\,k_BT\sigma$. This value is motivated by the condition that we want to prevent the polymers from collapsing by self-attraction. The persistence length also has to be larger than the simulation box height $L_p > 10\,\sigma$ to constrain the network to quasi-2d, while the formation of well-shaped vertices without large gaps requires a sufficiently low value of κ (see Fig. S5). In theory, one can deduce a *spring constant* k from the neglected fluctuation on the discretization length $b_0 = \sigma$ leading to a nearly inextensible polymer. We use the value $k = 100\,k_BT/b_0^2$ to mimic a practically inextensible polymer and keep the computational effort feasible [10]. We choose a *potential strength* $g = 0.7\,k_BT$ well above the critical value $g_c \lesssim 0.5\,k_BT$ to ensure that the bundling behaviour is not very sensitive with respect to the bending stiffness or the potential range $d = 1.4\,\sigma$ [5]. We perform another set of simulations with $g = 0.5\,k_BT$ to investigate if a weaker potential helps to avoid kinetically trapped states in simulations with square well pair potential (see Fig. 2f). The *length scale* of the LJ-potential is set to σ and the *energy scale* ε is computed from the condition of matching integrals over the attractive domains, i.e.

$$\int_{\sigma}^{r_c} \mathrm{d}r\, V_{LJ}(r) = -\,g(d-\sigma)\ ,$$

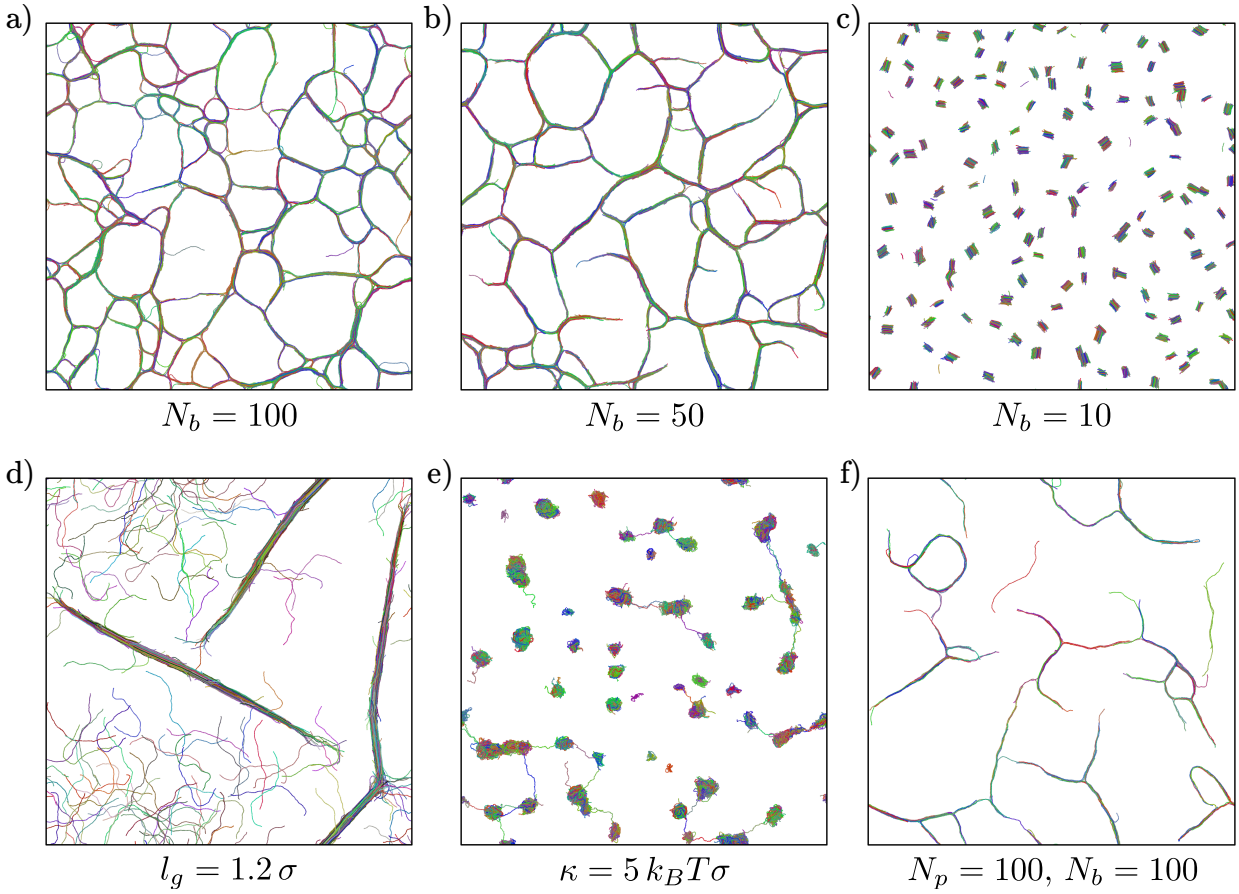

FIG. S4. ECMC simulations of mutually attractive SHC polymers in a simulation volume of size $400\,\sigma \times 400\,\sigma \times 10\,\sigma$. We vary different parameters of the simulations (number of beads per polymer N_b, range of the attractive square well interaction l_g, bending stiffness κ) one at a time to visualize their impact on the emerging structure. The snapshots a) to e) are created from simulations of 50 000 particles. a)-c): A reduction of the individual polymer length N_b does not change the structure significantly as long as $N_b\sigma > L_p \approx \kappa/k_BT = 30\,\sigma$. If $N_b\sigma < L_p$, the system evolves to many short, but unconnected bundles. d): A short-ranged attraction leads to the formation of few separate bundles with larger diameter instead of a volume-spanning meshed network. e): Very small bending stiffnesses κ are insufficient to keep the polymers in a straight conformation against their self-attraction and the systems forms several coils which would eventually merge to one large polymer coil. f): At low particle densities in the volume, the polymers are mostly able to adsorb to bundles, but there is no meshed network of these bundles.

where the LJ interaction is truncated at the cutoff length $r_c = 3\,\sigma$ in the simulations. With $g = 0.7\,k_BT$ and $d = 1.4\,\sigma$, we find the value $\varepsilon \approx 0.65\,k_BT$ used in our simulations.

III. IMAGE ANALYSIS METHODS

We apply methods from image analysis in order to extract properties of the bundled polymer network. Starting from a given configuration of the network, the bead positions are projected to the xy plane and subsequently rasterized, i.e., assigned to pixels (black pixels in Fig. S6).

Beads with less than three attractive overlaps (in the square well sense) are ignored at this stage, which effectively sets the lower limit of the bundle width to two polymers. A union-find algorithm is applied to the remaining pixels to identify clusters of pixels representing areas enclosed by the bundles (colored areas in Fig. S6). Very small pixel clusters like those associated with gaps at the center of some vertices (see Fig. 2 a)) are removed. To this end, the corresponding pixels are assigned to the bead pixels as if they were part of a bundle. Now, a skeletonization of the bead pixels representing the polymer bundles is performed to find vertices and the connecting edges. We aim to reduce the width of the bundles to one pixel by assigning bead pixels to the adjoining pixel clusters of the meshes. This process is continued as long as removal of the bead pixels does not change the topology of the mesh clusters,

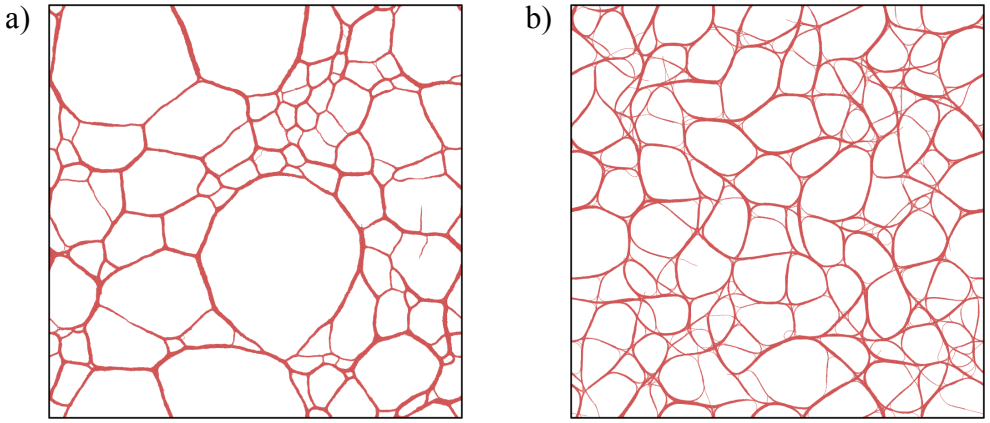

FIG. S5. MD simulations of 2800 polymers with different values of the bending stiffness, a) $\kappa = 30\,k_BT\sigma$ and b) $\kappa = 1000\,k_BT\sigma$. Both snapshots are created after 10^6 timesteps. Closer inspection of the vertices reveals the frequent occurrence of gaps at the network vertex positions for large values of κ.

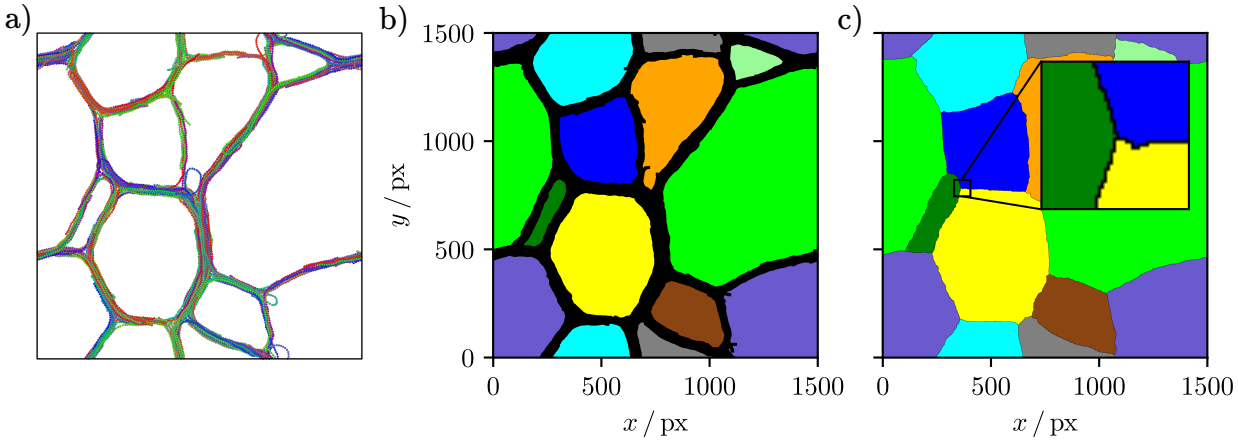

FIG. S6. Initial steps of the image analysis. a) This snapshot of a small simulation serves a an example to illustrate the different steps of the image analysis. b) Bead positions are projected to the xy plane and assigned to pixels (black pixels). The colors of the mesh pixel are arbitrary albeit unique. c) Pixel representation of the network after the skeletonization of the edge pixels.

i.e., creates gaps in the edges (Fig. S6). The remaining bead pixels can be associated with edges or vertices of the network based on the number of different colors of the adjoining pixels (see inset in Fig. S6). The logical structure of the vertex-edge system, i.e., which edge connects two vertices, is obtained by tracing the edge pixels that emanate from a vertex pixel. These steps are sufficient to determine an abstract representation the network structure (see Fig. S7). Many other steps of the analysis like the measurement of angles or the attribution of polymers to specific edges are based on this abstract representation.

a. Angles An estimate of the bundles bending angles at a vertex can be obtained from the direction of the (straight) edges (see Fig. S7). The bending angle φ_i is related to the inner mesh angle θ_i by $\pi = \varphi_\mathrm{i} + \theta_\mathrm{i}$. Effects arising from curvature in the bundles are neglected in this simple approach.

b. Topological information Adjacency information can be assigned to the edges since the edge pixels separate two pixel clusters of different color. These colors are used to identify meshes and their associated mesh clusters. The number of edges of a given mesh, which was previously denoted as n, is set by finding all edges that confine the mesh. This number is equivalent to the number of neighboring meshes. A potential source of inaccuracies arises when an edge length is similar to or smaller than the bundle width, i.e. for very short edges. In this case, the identification of the topological structure (which edge connects which vertices) is no longer unique and will in general depend on the details of the applied skeletonization procedure.

c. Attribution of polymers to edges The first step in the measurement of the subbundle sizes is the attribution of polymers to edges of the network structure. Beads can be associated with edges on the basis of a tessellation of the

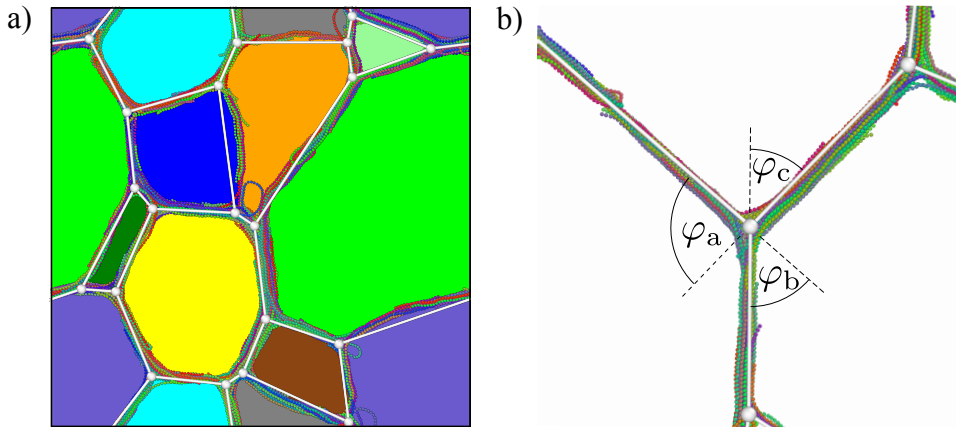

FIG. S7. a) Vertices and edges (white spheres and bonds) identified with the procedure outlined above. The corresponding polymer network is displayed as a reference. b) The measurement of the bending angles at the vertex is based on the edges and vertices.

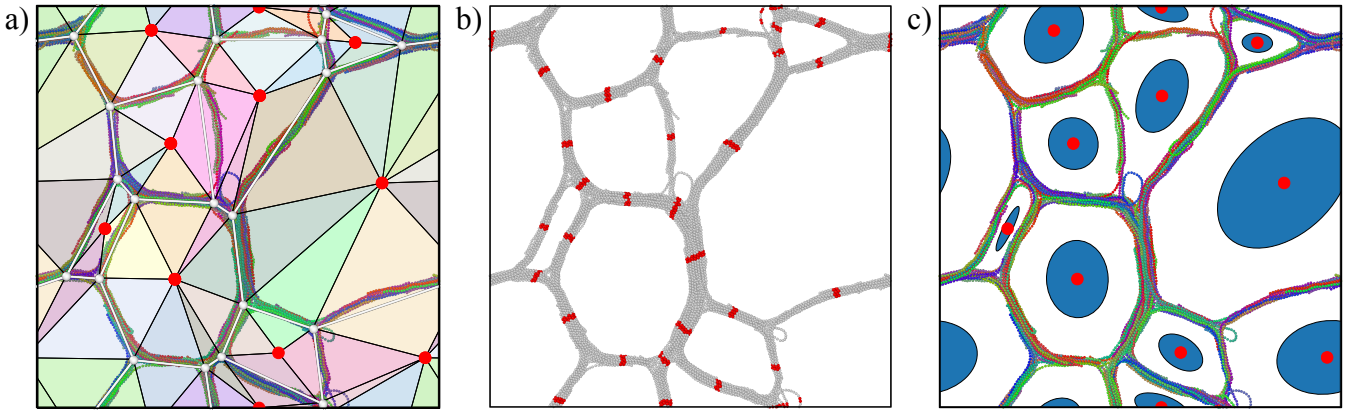

FIG. S8. a) Tessellation of the simulation volume with polygonal tiles (colored quadrilaterals) spanned by pairs of vertices (white dots) and the geometric centers of the adjacent meshes (red dots). b) Intersection beads (red) which are starting or end points while tracing polymers traversing a vertex. c) Ellipses of same area moments of inertia (blue) positioned at the meshes geometric center (red dots). For clarity, the ellipses are scaled by a factor of 0.5.

simulation volume. A polygonal tile is created for each edge where the polygon is spanned by the pair of connected vertices and the geometric centers of the adjacent meshes (see Fig. S8).

A bead is assigned to an edge if it is located within the tile. In order to find the polymers that constitute a subbundle, the polymers are traced starting from the center of the first edge to the center of one of the other two edges. Note that, in general, not all polymers reach one of the other edge centers. They might as well end on the way or return to the starting edge. To trace the path of a polymer, i.e. follow its bead sequence, the beads at the aforementioned edge centers must be defined. The location of the edge center is obtained from the pixel representation of the edge. Combined with the edge's direction, a plane is defined intersecting the polymer bundle. From the preselection made by the tessellation, all beads are determined whose tangent intersects the previously defined plane within a certain radius around the edge center. These beads are the *intersection beads* (see Fig. S8). Since it is known from the simulation data to which polymer a specific bead belongs, the path of polymers traversing a vertex can be traced and subbundles can be identified.

d. Pixel information Some mesh properties can be obtained directly from the pixel clusters. The area of a mesh corresponds to the number of pixels in the cluster and the circumference is the number of pixels that adjoin a bead pixel. Since the pixels also contain positional information, the meshes geometric center as well as the area moment of inertia tensor can be estimated. The latter one is used to quantify the asymmetry of the mesh shapes by finding ellipses that reproduce the eigenvalues of the second moment of area tensor (see Fig. S8 c)). Note that these quantities are measured prior to the skeletonization of the bead pixels.

IV. ISOLATED VERTICES

In this section, we consider simulations and analytical results for vertices of three mutually adsorbed subbundles without the surrounding network, so-called *isolated vertices*.

A. Isolated vertex simulation

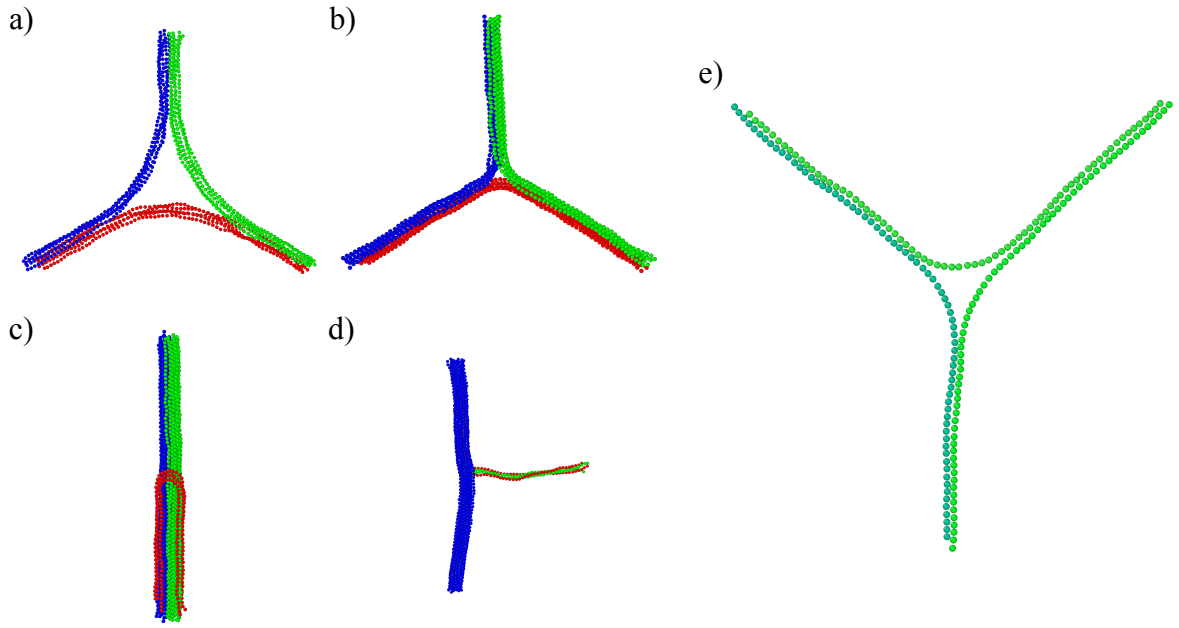

FIG. S9. Snapshots of isolated vertex simulations. Colors illustrate the assignment of polymers to subbundles. a) Initialization (hard sphere overlaps have been removed). b) Symmetric isolated vertex with $N_i = 5$. c, d) Limiting cases of $\Xi_a \to 0$ and $\Xi_a \to 1$. e) Polymer setup of a 2d isolated vertex simulation. This snapshot was taken from a simulation with symmetric subbundle sizes $\Xi_i = 1/3$.

Simulations of isolated vertices have several beneficial features aside from the considerably reduced computational cost due to the lower number of particles. Isolated vertex simulations allow us to determine the number of polymers for each subbundle, i.e., the relative subbundle sizes at the vertex, at simulation setup. Furthermore, isolated vertex simulations can be performed in genuine 2d, thus avoiding the influence of polymer rearrangements within the bundles on the relative angles between bundles. Angles measured in isolated vertex simulations seem to be well suited to compare predictions of theoretical models relating subbundle sizes to vertex angles. Conversely, isolated vertex simulations cannot capture the influence of the surrounding network on the angles.

In contrast to the isotropic initialization of the network simulations, the isolated vertex simulations start from a preformed vertex of three bundles of equal length, i.e. identical numbers of beads per polymer. The simulation box is a flat 3d volume similar to the network simulations. To set the subbundle sizes Ξ_i of the simulated vertex, the numbers of polymers of the respective bundle is adapted. Each bundle is initialized with two straight outer sections and a bend center section, where the center section has approximately the same length as both straight segments combined. In a next step, overlaps of the particles of diameter σ are removed producing a structure like Fig. S9a). Now, the pair potential is set to an attractive square well using parameters identical to the network simulation and the vertex structure is equilibrated. To measure the angles of the emerging vertex, we do not need to perform an image analysis because it is known from the initialization which polymer belongs to which bundle. Instead, the mean tangent is computed from the outer 20 beads of the polymers in each bundle and the bending angles are obtained from the scalar products of those tangent.

As stated above, isolated vertex simulations can also be performed in 2d simulation volumes. The particle positions for the initialization of the 2d simulation are generated similarly to the 3d case, but all positions are projected to the xy-plane. The main differences between 3d and 2d isolated vertices are that the particle movement during the simulation is constrained to the xy-plane and each bundle of the vertex is represented by a single polymer as illustrated

in Fig. S9 e). To emulate different subbundle sizes at the vertex, the bending constant of the polymers κ_i is adapted and the 2d relative subbundle size is redefined in terms of the bending constants

$$\Xi_i = \frac{\kappa_i}{\sum_j \kappa_j} \ .$$

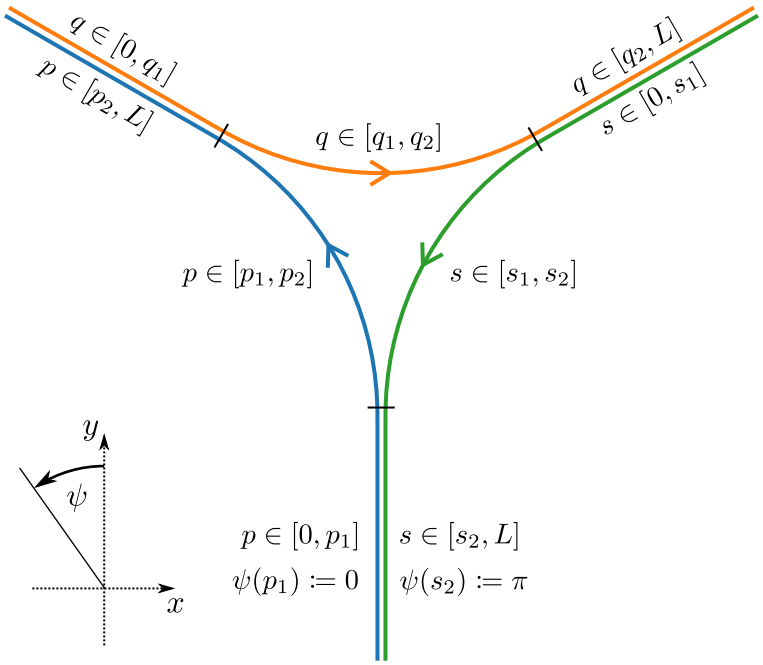

FIG. S10. Parameterisation of a vertex consisting of three WLCs (blue, orange and green). Colored arrows indicate the direction of the arc length parameterisation. Each polymer consists of two adsorbed, straight segments (bundle) and a curved segment at the vertex center. The direction of the y axis is chosen as the first straight segment of polymer p and angles ψ are measured with respect to y axis in mathematically positive direction.

B. Variational approach to the vertex model

The vertex model presented in the main text approximates the three subbundles as arcs of constant curvature within the domain of the vertex. The assumption of constant curvature can be justified starting from a Worm-Like-Chain (WLC) representation of the three mutually adsorbed subbundles involved in a vertex. A variation of the polymer contours parameterised with respect to the arc length will result in solutions of constant curvature for each WLC (i.e. subbundle) only in the limit of a symmetric vertex. We show that constant curvature arcs remain a good approximation also in the presence of asymmetry (i.e., differences in the three subbundle sizes).

1. *Formulation of the variational problem*

As a simplified model for the calculation, we consider three polymers p, q and s of equal length L and free ends in the xy plane. The contours are described by angles ψ as a function of the respective arc length, e.g. $\psi(p_1)$ denotes the angle of polymer p at arc length p_1 (see Fig. S10). Contact points of the polymers are denoted with subscripts 1 and 2; for example, the arc length interval of the curved segment for polymer p is $p \in [p_1, p_2]$. We also implicitly assume a sufficiently strong attraction among the polymers to ensure the existence of the straight segments as well as pairwise parallel ends at the bundle termini. Therefore, we obtain the energy expression

$$\begin{aligned}\mathcal{H}\left[\psi(p), \psi(q), \psi(s)\right] = \sum_{u \in \{p,q,s\}} \Bigg[&\int_0^{u_1} \mathrm{d}u \left(\frac{\kappa_u}{2} \left(\frac{\partial \psi}{\partial u} \right)^2 - \gamma_{1,u} \right) + \int_{u_1}^{u_2} \mathrm{d}u \, \frac{\kappa_u}{2} \left(\frac{\partial \psi}{\partial u} \right)^2 \\ &+ \int_{u_2}^{L} \mathrm{d}u \left(\frac{\kappa_u}{2} \left(\frac{\partial \psi}{\partial u} \right)^2 - \gamma_{2,u} \right) \Bigg] ,\end{aligned} \tag{1}$$

with bending rigidities κ_u and an attraction per unit length $\gamma_{1/2,u}$. Clearly, the attractive strength within an adsorbed segment should be equal for both polymers, e.g. $\gamma_{1,p} = \gamma_{2,s}$. The energy expression (1) does not inherently guarantee a closed vertex shape. We therefore introduce two constraints of zero net-displacements for one complete cycle through

the vertex

$$0 \stackrel{!}{=} \Delta x = \sum_{u\in\{p,q,s\}} \Delta x_u = -\sum_{u\in\{p,q,s\}} \int_{u_1}^{u_2} \mathrm{d}u\, \sin(\psi)$$
$$0 \stackrel{!}{=} \Delta y = \sum_{u\in\{p,q,s\}} \Delta y_u = \sum_{u\in\{p,q,s\}} \int_{u_1}^{u_2} \mathrm{d}u\, \cos(\psi)\ .$$

To find the stationary configuration of (1) subject to the constraints, we vary $\mathcal{L} = \mathcal{H} + \lambda_x \Delta x + \lambda_y \Delta y$ with respect to ψ as well as the contact points $u_{1/2}$ and take into account the interconnection between the variations of the angle at the endpoints and the variation of the contact points $\delta\psi_{u_i} := \delta\psi(u_i) + \partial\psi/\partial u|_{u_i}\Delta u_i$

$$\begin{aligned}
\delta\mathcal{L} = \sum_{u\in\{p,q,s\}} \Bigg\{ & -\int_0^{u_1} \mathrm{d}u\, \left[\kappa_u \frac{\partial^2\psi}{\partial u^2}\delta\psi(u)\right] + \kappa_u \frac{\partial\psi}{\partial u}\bigg|_{u=u_1^-}\delta\psi_{u_1^-} - \kappa_u \frac{\partial\psi}{\partial u}\bigg|_{u=0}\delta\psi(0) \\
& - \left(\frac{\kappa_u}{2}\left(\frac{\partial\psi}{\partial u}\right)^2 + \gamma_{1,u}\right)\bigg|_{u=u_1^-}\Delta u_1^- \\
& - \int_{u_1}^{u_2} \mathrm{d}u\, \left[\kappa_u \frac{\partial^2\psi}{\partial u^2} + \lambda_x\cos(\psi) + \lambda_y\sin(\psi)\right]\delta\psi(u) \\
& + \kappa_u \frac{\partial\psi}{\partial u}\bigg|_{u=u_2^-}\delta\psi_{u_2^-} - \kappa_u \frac{\partial\psi}{\partial u}\bigg|_{u=u_1^+}\delta\psi_{u_1^+} \\
& - \left(\frac{\kappa_u}{2}\left(\frac{\partial\psi}{\partial u}\right)^2 + \lambda_x\sin(\psi) - \lambda_y\cos(\psi)\right)\bigg|_{u=u_2^-}\Delta u_2^- \\
& + \left(\frac{\kappa_u}{2}\left(\frac{\partial\psi}{\partial u}\right)^2 + \lambda_x\sin(\psi) - \lambda_y\cos(\psi)\right)\bigg|_{u=u_1^+}\Delta u_1^+ \\
& - \int_{u_2}^{L} \mathrm{d}u\, \left[\kappa_u \frac{\partial^2\psi}{\partial u^2}\delta\psi(u)\right] + \kappa_u \frac{\partial\psi}{\partial u}\bigg|_{u=L}\delta\psi(L) - \kappa_u \frac{\partial\psi}{\partial u}\bigg|_{u=u_2^+}\delta\psi_{u_2^+} \\
& + \left(\frac{\kappa_u}{2}\left(\frac{\partial\psi}{\partial u}\right)^2 + \gamma_{2,u}\right)\bigg|_{u=u_2^+}\Delta u_2^+ \Bigg\}\ ,
\end{aligned}$$

where the superscript $\pm$ means that the contact points are approached from above and below, respectively. We demand the polymer contours to be continuous $\Delta u_i^+ = \Delta u_i^- = \Delta u_i$ and smooth $\delta\psi_{u_i^+} = \delta\psi_{u_i^-} = \delta\psi_{u_i}$ at the contact points. Moreover, the variations at the contact points are coupled in pairs

$$\begin{array}{lll}
\delta\psi_{p_1} = \delta\psi_{s_2} & \delta\psi_{q_1} = \delta\psi_{p_2} & \delta\psi_{s_1} = \delta\psi_{q_2} \\
\Delta p_1 = -\Delta s_2 & \Delta q_1 = -\Delta p_2 & \Delta s_1 = -\Delta q_2\ ,
\end{array}$$

where the minus signs arise from the mutually opposite orientations of the polymers. The variation of $\mathcal{L}$ thus obtained reads

$$
\begin{aligned}
\delta\mathcal{L} = \sum_{u\in\{p,q,s\}} \Bigg\{ & -\int_0^{u_1} \mathrm{d}u \left[\kappa_u \frac{\partial^2\psi}{\partial u^2}\delta\psi(u)\right] - \int_{u_1}^{u_2} \mathrm{d}u \left[\kappa_u \frac{\partial^2\psi}{\partial u^2} + \lambda_x\cos(\psi) + \lambda_y\sin(\psi)\right]\delta\psi(u) \\
& - \int_{u_2}^{L} \mathrm{d}u \left[\kappa_u \frac{\partial^2\psi}{\partial u^2}\delta\psi(u)\right] + \kappa_u \frac{\partial\psi}{\partial u}\Big|_{u=L}\delta\psi(L) - \kappa_u \frac{\partial\psi}{\partial u}\Big|_{u=0}\delta\psi(0) \Bigg\} \\
& + \left[\kappa_p\left(\frac{\partial\psi}{\partial p}\Big|_{p_1^-} - \frac{\partial\psi}{\partial p}\Big|_{p_1^+}\right) + \kappa_s\left(\frac{\partial\psi}{\partial s}\Big|_{s_2^-} - \frac{\partial\psi}{\partial s}\Big|_{s_2^+}\right)\right]\delta\psi_{p_1} \\
& + \left[\kappa_q\left(\frac{\partial\psi}{\partial q}\Big|_{q_1^-} - \frac{\partial\psi}{\partial q}\Big|_{q_1^+}\right) + \kappa_p\left(\frac{\partial\psi}{\partial p}\Big|_{p_2^-} - \frac{\partial\psi}{\partial p}\Big|_{p_2^+}\right)\right]\delta\psi_{q_1} \\
& + \left[\kappa_s\left(\frac{\partial\psi}{\partial s}\Big|_{s_1^-} - \frac{\partial\psi}{\partial s}\Big|_{s_1^+}\right) + \kappa_q\left(\frac{\partial\psi}{\partial q}\Big|_{q_2^-} - \frac{\partial\psi}{\partial q}\Big|_{q_2^+}\right)\right]\delta\psi_{s_1} \\
& - \Bigg[\gamma_{1,p} + \frac{\kappa_p}{2}\left(\frac{\partial\psi}{\partial p}\Big|_{p_1^-}\right)^2 - \frac{\kappa_p}{2}\left(\frac{\partial\psi}{\partial p}\Big|_{p_1^+}\right)^2 - \lambda_x\sin(\psi)\big|_{p_1^+} + \lambda_y\cos(\psi)\big|_{p_1^+} \\
& \quad - \frac{\kappa_s}{2}\left(\frac{\partial\psi}{\partial s}\Big|_{s_2^-}\right)^2 + \gamma_{2,s} + \frac{\kappa_s}{2}\left(\frac{\partial\psi}{\partial s}\Big|_{s_2^+}\right)^2 - \lambda_x\sin(\psi)\big|_{s_2^-} + \lambda_y\cos(\psi)\big|_{s_2^-}\Bigg]\Delta p_1 \\
& - \Bigg[\gamma_{1,q} + \frac{\kappa_q}{2}\left(\frac{\partial\psi}{\partial q}\Big|_{q_1^-}\right)^2 - \frac{\kappa_q}{2}\left(\frac{\partial\psi}{\partial q}\Big|_{q_1^+}\right)^2 - \lambda_x\sin(\psi)\big|_{q_1^+} + \lambda_y\cos(\psi)\big|_{q_1^+} \\
& \quad - \frac{\kappa_p}{2}\left(\frac{\partial\psi}{\partial p}\Big|_{p_2^-}\right)^2 + \gamma_{2,p} + \frac{\kappa_p}{2}\left(\frac{\partial\psi}{\partial p}\Big|_{p_2^+}\right)^2 - \lambda_x\sin(\psi)\big|_{p_2^-} + \lambda_y\cos(\psi)\big|_{p_2^-}\Bigg]\Delta q_1 \\
& - \Bigg[\gamma_{1,s} + \frac{\kappa_s}{2}\left(\frac{\partial\psi}{\partial s}\Big|_{s_1^-}\right)^2 - \frac{\kappa_s}{2}\left(\frac{\partial\psi}{\partial s}\Big|_{s_1^+}\right)^2 - \lambda_x\sin(\psi)\big|_{s_1^+} + \lambda_y\cos(\psi)\big|_{s_1^+} \\
& \quad - \frac{\kappa_q}{2}\left(\frac{\partial\psi}{\partial q}\Big|_{q_2^-}\right)^2 + \gamma_{2,q} + \frac{\kappa_q}{2}\left(\frac{\partial\psi}{\partial q}\Big|_{q_2^+}\right)^2 - \lambda_x\sin(\psi)\big|_{q_2^-} + \lambda_y\cos(\psi)\big|_{q_2^-}\Bigg]\Delta s_1 \\
\stackrel{!}{=} & \, 0 \,,
\end{aligned}
\tag{2}
$$

where the lines proportional to $\delta\psi$ and Δu are the Weierstrass-Erdmann conditions. The boundary conditions on the angles at the contact points

$$
\psi(p_1) = \psi(s_2) - \pi \qquad \psi(q_1) = \psi(p_2) - \pi \qquad \psi(s_1) = \psi(q_2) + \pi
$$

can be used to cancel out the $\sin(\psi)$ and $\cos(\psi)$ contributions in the Weierstrass-Erdmann conditions, e.g.

$$
\lambda_x\left(\sin(\psi)\big|_{\alpha_1} + \sin(\psi)\big|_{\beta_2}\right) = \lambda_x\left(\sin(\psi)\big|_{\alpha_1} + \sin(\psi\pm\pi)\big|_{\alpha_1}\right) = 0 \,.
$$

We demand the first variation to vanish $\delta\mathcal{L} \stackrel{!}{=} 0$ and from the integrals we obtain for the adsorbed segments $i = 1, 3$ of the polymer the differential equation

$$
0 = \kappa_u \frac{\partial^2\psi}{\partial u^2} \quad \stackrel{\kappa_u\neq 0}{\Longrightarrow} \quad \psi(u) = c_1^{i,u}u + c_2^{i,u} \tag{3}
$$

with constants $c_{1/2}^{i,u}$ yet to be determined. The polymer segments of the junction section obey the more complicated equation

$$
0 = \kappa_u \frac{\partial^2\psi}{\partial u^2} + \lambda_x\cos(\psi) + \lambda_y\sin(\psi) \,, \tag{4}
$$

which does not have a simple analytic solution in the general case albeit a first integral can be found

$$\left(\frac{\partial\psi}{\partial u}\right)^2 = -2\frac{\lambda_x}{\kappa_u}\sin(\psi) + 2\frac{\lambda_y}{\kappa_u}\cos(\psi) + \frac{d_u}{\kappa_u}$$

with the integration constant d_u. The differential equations (3) and (4) are equivalent for $\lambda_x = \lambda_y = 0$ and the bent center section of the polymer contours become arcs of constant curvature in this case. A solution with vanishing Lagrange parameters must fulfill the constraints $\Delta x = \Delta y = 0$ trivially and this is exactly the case for a fully symmetric vertex. We expect the $\lambda_{x/y}$ to vary continuously with respect to the vertex parameters and, therefore, a small asymmetry of the parameters κ_u and $\gamma_{1/2,u}$ should yield Lagrange parameters close to zero. In that limit, we could use a perturbation approach to solve the differential equation. However, the asymmetry of vertices observed in simulations is generally not very small and instead of a perturbation expansion we solve (4) numerically. The solution thus obtained is compared to the zeroth order perturbation solution assuming a constant curvature in the following Sec. IV C.

The model described in this section considers an isolated vertex without surrounding network, that is the angles at the termini of each polymer can be adjusted freely to minimize the energy. Consequently, the variations at the endpoints do not have to vanish $\delta\psi(0) \neq 0$ and $\delta\psi(L) \neq 0$. The condition $\delta\mathcal{L} = 0$ therefore implies for each polymer $u \in \{p, q, s\}$

$$0 = \kappa_u \frac{\partial\psi}{\partial u}\Big|_{u=L} = \kappa_u \frac{\partial\psi}{\partial u}\Big|_{u=0} \quad \overset{\psi(u)=c_1^{i,u}u+c_2^{i,u}}{\Longrightarrow} \quad c_1^{1,u} = c_1^{3,u} = 0\ ,$$

bearing the intuitively obvious result that the outer (adsorbed) sections of the free vertex are in a straight conformation. Using this finding to set $\partial\psi/\partial u|_{u_1^-} = \partial\psi/\partial u|_{u_2^+} = 0$, we obtain from the variations of the angles at the contact points (terms $[\cdots]\delta\psi|_{u_1}$ in (2)) conditions for the mechanical equilibrium of the stationary vertex configuration

$$\kappa_p \frac{\partial\psi}{\partial p}\Big|_{p_1^+} = \kappa_s \frac{\partial\psi}{\partial s}\Big|_{s_2^-} \qquad \kappa_q \frac{\partial\psi}{\partial q}\Big|_{q_1^+} = \kappa_p \frac{\partial\psi}{\partial p}\Big|_{p_2^-} \qquad \kappa_s \frac{\partial\psi}{\partial s}\Big|_{s_1^+} = \kappa_q \frac{\partial\psi}{\partial q}\Big|_{q_2^-}\ . \tag{5}$$

Using the mechanical equilibrium conditions as well as the previous result $\partial\psi/\partial u|_{u_1^-} = \partial\psi/\partial u|_{u_2^+} = 0$, we can derive the contact curvature at the junctions from the terms proportional to Δu_1 in (2) for $u \in \{p, q, s\}$

$$\left(\frac{\partial\psi}{\partial p}\Big|_{p_1^+}\right)^2 = \frac{2\left(\gamma_{1,p}+\gamma_{2,s}\right)}{\kappa_s+\kappa_p}\,\frac{\kappa_s}{\kappa_p} \qquad \left(\frac{\partial\psi}{\partial s}\Big|_{s_2^-}\right)^2 = \frac{2\left(\gamma_{1,p}+\gamma_{2,s}\right)}{\kappa_s+\kappa_p}\,\frac{\kappa_p}{\kappa_s}$$
$$\left(\frac{\partial\psi}{\partial q}\Big|_{q_1^+}\right)^2 = \frac{2\left(\gamma_{1,q}+\gamma_{2,p}\right)}{\kappa_p+\kappa_q}\,\frac{\kappa_p}{\kappa_q} \qquad \left(\frac{\partial\psi}{\partial p}\Big|_{p_2^-}\right)^2 = \frac{2\left(\gamma_{1,q}+\gamma_{2,p}\right)}{\kappa_p+\kappa_q}\,\frac{\kappa_q}{\kappa_p}$$
$$\left(\frac{\partial\psi}{\partial s}\Big|_{s_1^+}\right)^2 = \frac{2\left(\gamma_{1,s}+\gamma_{2,q}\right)}{\kappa_q+\kappa_s}\,\frac{\kappa_q}{\kappa_s} \qquad \left(\frac{\partial\psi}{\partial q}\Big|_{q_2^-}\right)^2 = \frac{2\left(\gamma_{1,s}+\gamma_{2,q}\right)}{\kappa_q+\kappa_s}\,\frac{\kappa_s}{\kappa_q}\ .$$

To compute the vertex shape, i.e. a set of unique solutions of the differential equation (4), we need a total of eight boundary conditions six of which are the contact curvatures. To proceed, one would typically use the constraints $0 = \Delta x = \Delta y$ as additional conditions to fix the Lagrange parameters $\lambda_{x/y}$. However, a short calculation reveals an interdependence of the two constraints of net-zero displacement and the mechanical equilibrium. We start from the superposition

$$\lambda_x\Delta y + \lambda_y\Delta x = \sum_{u\in\{p,q,s\}} \int_{u_1}^{u_2} \mathrm{d}u\left[\lambda_x\cos(\psi) + \lambda_y\sin(\psi)\right]\ .$$

Because ψ is a solution of (4) and $\psi = \psi(u)$ depends only on the respective arc length position, we obtain

$$\begin{aligned}\lambda_x\Delta y + \lambda_y\Delta x &= \sum_{u\in\{p,q,s\}} \int_{u_1}^{u_2} \mathrm{d}u\,(-\kappa_u)\,\frac{\partial^2\psi}{\partial u^2} \\ &= \sum_{u\in\{p,q,s\}} \left[-\kappa_u\frac{\partial\psi}{\partial u}\Big|_{u_2^-} + \kappa_u\frac{\partial\psi}{\partial u}\Big|_{u_1^+}\right] \overset{(5)}{=} 0\ .\end{aligned}$$

The terms of the sum in the last line always cancel out pairwise if the conditions of mechanical equilibrium are met. Therefore, we use $0 = \Delta x - \Delta y$ as one additional condition. The last degree of freedom can be fixed by choosing the coordinate system and we arbitrarily set $\psi(p_1) = 0$ which implies $\psi(s_2) = \pi$.

2. Model parameters as a function of the relative subbundle sizes

To compare the angles predicted by the vertex model to simulation data from isolated vertices or, in particular, entire networks, we have to express the model parameters κ_u and $\gamma_{1/2,u}$ in terms of the relative subbundle sizes $\Xi_u = N_u/N_{tot}$, where $N_{tot} = \sum_j N_j$ is the total number of polymers traversing the vertex. The assumption of decoupled bending motivated by the polymers ability to slide along a bundle yields

$$\kappa_u \approx N_u \kappa = \Xi_u N_{tot} \kappa \, .$$

The energy reduction during adsorption of two bundles is due to the reduction of bundle surface and we therefore expect a relation

$$\gamma_{u,l} \approx \sqrt{N_u + N_l}\gamma = \sqrt{(\Xi_u + \Xi_l)N_{tot}}\gamma \, ,$$

where u and l denote the two polymers or bundles in contact, e.g. polymer $u = s$ and $l = q$. We rewrite the contact curvatures with these definitions as

$$\left(\frac{\partial \psi}{\partial p}\bigg|_{p_1^+} \right)^2 = \frac{4\gamma}{\kappa\sqrt{(\Xi_s + \Xi_p)N_{tot}}} \frac{\Xi_s}{\Xi_p} \qquad \left(\frac{\partial \psi}{\partial s}\bigg|_{s_2^-} \right)^2 = \frac{4\gamma}{\kappa\sqrt{(\Xi_s + \Xi_p)N_{tot}}} \frac{\Xi_p}{\Xi_s}$$

and similarly for the other contact points. These contact curvatures define a characteristic length scale l for the given set of vertex parameters

$$l^2 = \frac{\kappa\sqrt{N_{tot}}}{2\gamma} \, ,$$

which is used to non-dimensionalize the differential equation for subsequent numerical treatment. After rescaling the differential equation (4) with l^2, we find

$$\frac{\partial^2 \psi}{\partial \tilde{u}^2} = -\frac{\lambda_x}{2\gamma\Xi_u\sqrt{N_{tot}}}\cos(\psi) - \frac{\lambda_y}{2\gamma\Xi_u\sqrt{N_{tot}}}\sin(\psi) \tag{6}$$

with a dimensionless length $\tilde{u} = u/l$ and dimensionless Lagrange parameters $\tilde{\lambda}_{x/y} = \lambda_{x/y}/2\gamma\sqrt{N_{tot}}$. A similar rescaling of the contact curvature shows that the differential equation (6) as well as the contact curvatures become independent of N_{tot}. The vertex angles $\psi(u_2)$ are consequently independent of the total number of polymers in the vertex N_{tot} and, instead, depend only on the relative distribution of those polymers to the subbundles. The arc length interval of the vertex junction scales as $u = l\tilde{u} \sim N_{tot}^{1/4}$.

3. Numerical integration of the vertex contour

While the conditions stated in the paragraphs above are sufficient to define a unique solution of the differential equations, an implementation of a numerical routine to actually compute this solution requires knowledge of the arc length coordinates of the contact points $u_{1/2}$, which are not known a priori. This problem can be alleviated by a shift of the arc length coordinates $\hat{u} = \tilde{u} - \tilde{u}_1$ such that $\hat{u}(\tilde{u}_1) = 0$ at the first contact point. The remaining quantities $\hat{p}_2$, $\hat{q}_2$, $\hat{s}_2$, $\tilde{\lambda}_x$ and $\tilde{\lambda}_y$ are treated as shooting parameters of a (multidimensional) boundary value problem. Our numerical procedure works as follows:

1. Starting from $\psi(\hat{p} = 0) = 0$ and the known value of the contact curvature $\partial\psi/\partial\hat{p}|_{\hat{p}_1^+=0}$, we integrate $\psi(\hat{p})$ using the initial guess (or the result of the previous iteration) of the shooting parameters.

2. With the computed value of $\psi(\hat{p}_2)$, we integrate $\psi(\hat{q})$ with the initial values $\psi(\hat{q}_1 = 0) = \psi(\hat{p}_2) - \pi$ and the contact curvature. Similarly, we compute $\psi(\hat{s})$ with the help of $\psi(\hat{q}_2)$.

3. The approximate solutions ψ thus obtained allow to quantify the deviation to the boundary values. We reformulate the equation as a root-finding problem

$$\vec{0} \stackrel{!}{=} \begin{pmatrix} c_{\hat{p}_2^-} \\ c_{\hat{q}_2^-} \\ c_{\hat{s}_2^-} \\ 0 \\ \pi \end{pmatrix} - \begin{pmatrix} \partial\psi/\partial\hat{p}\big|_{\hat{p}_2^-} \\ \partial\psi/\partial\hat{q}\big|_{\hat{q}_2^-} \\ \partial\psi/\partial\hat{s}\big|_{\hat{s}_2^-} \\ \Delta\tilde{x} - \Delta\tilde{y} \\ \psi(\hat{s}_2) \end{pmatrix} \, ,$$

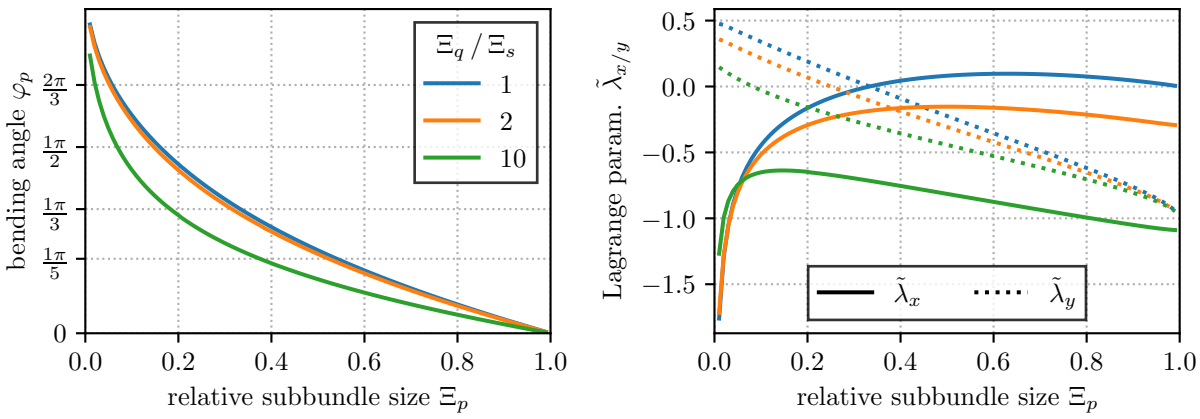

FIG. S11. Predictions obtained from the vertex model described above for different vertex configurations characterized by the relative subbundle sizes Ξ_u. Left: Bending angles $\varphi_p = \psi(p_2)$ for different levels of asymmetry Ξ_q/Ξ_s (colors). Right: Associated values of the Lagrange parameters $\tilde{\lambda}_{x/y}$ as a function of Ξ_p for different levels of asymmetry (colors).

where $c_{\hat{u}_2^-}$ denotes the contact curvatures at the second contact point. The root-finding algorithm generates a new guess for the shooting parameters and the iteration starts over.

Once the iteration procedure has converged, we use the model assumptions of parallel polymer ends and equal lengths to compute the arc length positions of the first contact points. For each polymer, we have an equation of the form $\tilde{p}_1 + \hat{p}_2 = L/l - \tilde{q}_1$ and similarly for q and s. This system of linear equations is solved for the contact points and we find

$$\tilde{p}_1 = \frac{\tilde{L} - \hat{p}_2 - \hat{s}_2 + \hat{q}_2}{2} \qquad \tilde{q}_1 = \frac{\tilde{L} - \hat{q}_2 - \hat{p}_2 + \hat{s}_2}{2} \qquad \tilde{s}_1 = \frac{\tilde{L} - \hat{s}_2 - \hat{q}_2 + \hat{p}_2}{2}\,.$$

We are now in a position to predict bending angles $\varphi_u = \psi(u_2) - \psi(u_1)$ as a function of the relative subbundle sizes Ξ_u. Fig. S11 shows the angles thus obtained for different ratios Ξ_q/Ξ_s characterizing the asymmetry.

The computed angles are compatible with the limiting cases $\lim_{\Xi_p\to 1}\psi(p_2) = 0$ and $\lim_{\Xi_p\to 0}\psi(p_2) = \pi$ for all ratios Ξ_q/Ξ_s. Additionally, we can reproduce the known result for the fully symmetric vertex $\psi(p_2) = \pi/3$ with equal subbundle sizes $\Xi_p = \Xi_q = \Xi_s = 1/3$. The magnitude of the Lagrange parameters $\tilde{\lambda}_{x/y}$ allows to assess the deviation of the computed contour from arcs of constant curvature. We find from Fig. S11 a tendency of increasing $|\tilde{\lambda}_{x/y}|$ for increasing asymmetry of the vertex. A vertex becomes asymmetric in the limits $\Xi_u \to 0$ and $\Xi_u \to 1$ or for large ratios Ξ_q/Ξ_s of the subbundle sizes. Fig. S11 also shows that the size of the opposing subbundles has surprisingly little effect on the angle φ_p. The difference between $\varphi_p|_{\Xi_q=\Xi_s}$ and $\varphi_p|_{\Xi_q=2\Xi_s}$ is barely recognisable from the figure. Albeit a more pronounced difference is observed for $\Xi_q/\Xi_s = 10$, one should keep in mind that such large ratios of subbundle sizes and equivalently the number of polymers in subbundles are rather exotic given the homogeneous initialization of the simulated system.

C. Comparison to vertex model of circular arcs

The vertex model presented in the main text that approximates the subbundles as arcs of constant curvature can be generalized to non-symmetric vertices. Clearly, the energy contribution per subbundle is unchanged

$$\frac{2E_u}{\kappa N_{tot}} = \frac{L_u N_u}{R_u^2 N_{tot}} + \frac{2g}{\kappa} L_u \frac{\sqrt{N_u}}{N_{tot}} = \frac{\varphi_u}{R_u}\Xi_u + \frac{2g}{\kappa}\varphi_u R_u \sqrt{\frac{\Xi_u}{N_{tot}}}\,,$$

where the first term $\propto N_u$ describes the decoupled bending of N_u polymers and the second term $\propto \sqrt{N_u}$ missing attractive overlaps on the bundle surface. To estimate the size of the bundle surface, we approximate the (sub-)bundle u as cylinder of length L_u and cross-sectional area $\sim \sigma^2 N_u$ with polymer diameter σ. A comparison of the typical spatial size of a vertex to the length of the polymers $L_{poly} \approx 100\,\sigma$ shows that $L_u < L_{poly}$ and we assume all N_u polymers to fully traverse the subbundle. These arguments lead to a side area $S \sim \sqrt{N_u} L_u$.

The law of cosines allows to rewrite the angles φ_u as functions of the edge lengths of the corresponding triangle (see sketch in the main text Fig. 2a), which effectively translates into expressing the angles as functions of the R_u. However, enforcing the law of cosines and thereby the triangular properties via Lagrange multipliers proves to be preferable for reasons of numerical stability, as it eliminates the need to invert trigonometric functions. Overall, we aim to minimize the expression

$$\begin{aligned}\mathcal{L} = &\sum_{u\in\{p,q,s\}} \varphi_u \left(\frac{\Xi_u}{R_u} + \frac{2g}{\kappa} R_u \sqrt{\frac{\Xi_u}{N_{tot}}}\right) \\ &+ \lambda_1 \left[(R_q + R_p)\cos(\varphi_q) + (R_p + R_s)\cos(\varphi_s) - R_s - R_q\right] \\ &+ \lambda_2 \left[(R_s + R_q)\cos(\varphi_s) + (R_p + R_q)\cos(\varphi_p) - R_p - R_s\right] \\ &+ \lambda_3 \left[(R_p + R_s)\cos(\varphi_p) + (R_s + R_q)\cos(\varphi_q) - R_q - R_p\right] \ ,\end{aligned} \tag{7}$$

where λ_i denote the Lagrange multipliers introduced for the law of cosines. Optimizing $\mathcal{L}$ with respect to φ and R yields the conditions

$$\begin{aligned}\frac{\partial \mathcal{L}}{\partial \varphi_p} &= \frac{\Xi_p}{R_p} + \frac{2g}{\kappa} R_p \sqrt{\frac{\Xi_p}{N_{tot}}} - \lambda_2 (R_p + R_q)\sin(\varphi_p) - \lambda_3 (R_p + R_s)\sin(\varphi_p) \stackrel{!}{=} 0 \\ \frac{\partial \mathcal{L}}{\partial R_p} &= -\frac{\varphi_p \Xi_p}{R_p^2} + \frac{2g}{\kappa}\varphi_p \sqrt{\frac{\Xi_p}{N_{tot}}} + \lambda_1 \left[\cos(\varphi_q) + \cos(\varphi_s)\right] + \lambda_2 \left[\cos(\varphi_p) - 1\right] + \lambda_3 \left[\cos(\varphi_p) - 1\right] \stackrel{!}{=} 0\end{aligned}$$

and similar equations for the quantities with subscripts q and s. These six conditions combined with the three constraints (square brackets in (7)) define the necessary conditions for the minimal $\mathcal{L}$. In order to compute the angles and radii from the multidimensional root-finding problem with a numerical procedure, we non-dimensionalize the equation with a characteristic length scale given by

$$l^2 = \frac{\kappa\sqrt{N_{tot}}}{2g}$$

(we note that the energy $2E/\kappa N_{tot}$ has dimension of inverse length). Written in terms of the dimensionless quantities $\tilde{\mathcal{L}} = l\mathcal{L}$, $R = \tilde{R}l$ and $\tilde{\lambda} = l^2\lambda$, the factor $2g/\kappa\sqrt{N_{tot}}$ drops out of the equations, e.g.

$$\frac{\partial \tilde{\mathcal{L}}}{\partial \varphi_p} = \frac{\Xi_p}{\tilde{R}_p} + \tilde{R}_p\sqrt{\Xi_p} - \tilde{\lambda}_2(\tilde{R}_p + \tilde{R}_q)\sin(\varphi_p) - \tilde{\lambda}_3(\tilde{R}_p + \tilde{R}_s)\sin(\varphi_p) = 0 \ .$$

Similar to the full variational calculation for the isolated vertex model presented in the previous section we find the angles to be independent of the total number of polymers in the vertex N_{tot} and the lengths of the bent arcs scale as $L_i = R_i\varphi_i = l\tilde{R}_i\varphi_i \sim N_{tot}^{1/4}$. A comparison of the results of the full variational calculation and the circular arc approximation for the angles $\varphi_u = \psi(u_2) - \psi(u_1)$ is shown in Fig. S12 for different ratios of the subbundle sizes Ξ_q/Ξ_s.

We obtain quantitatively very similar results for the entire range of subbundle sizes even for the most asymmetric subbundle size ratio $\Xi_q/\Xi_s = 10$. This motivates our choice to present the simplified vertex model assuming circular arcs in the main text for reasons of conciseness.

The model predictions of the bending angle φ_p (in the circular arc approximation, but practically identical to the full variational approach) is compared to measurements from isolated vertex simulations in Fig. S13. We perform 3d isolated vertex simulations in a flat 3d volume similar to the network simulations for the subbundle size ratio $\Xi_q = 2\,\Xi_s$ and 2d isolated vertex simulations for the subbundle size ratio $\Xi_q = 10\,\Xi_s$, because such a vertex configuration requires the simulation of a large number of polymers, e.g. for $\Xi_p = 0.9$ with $N_q = 10$, $N_s = 1$ (i.e. $\Xi_q/\Xi_s = 10$) implies the total number of polymers $N_{tot} = 110$. For both simulation geometries we find good agreement with the 2d circular arc approximation. The observed angles agree particularly well for large subbundle sizes $\Xi_p \geq 0.3$ and larger deviations are observed only in the range $\Xi_p \leq 0.05$.

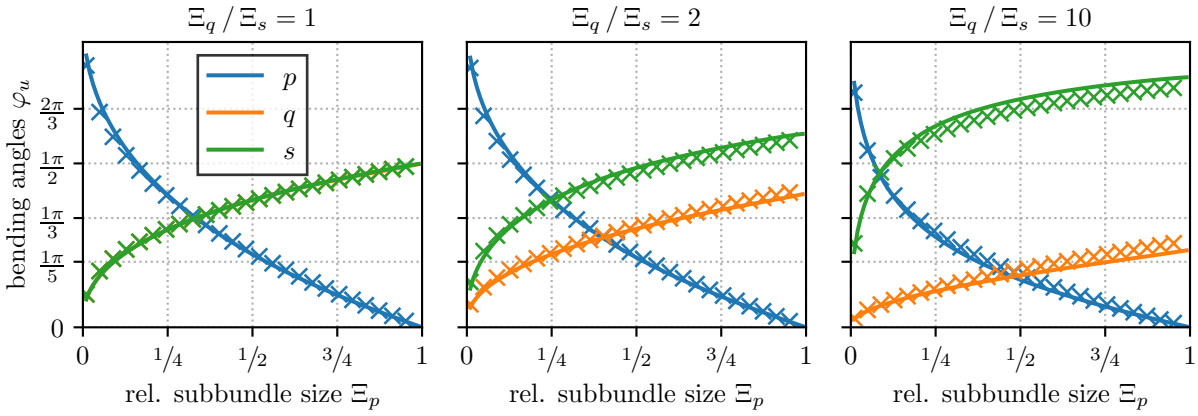

FIG. S12. Bending angles φ_u of the subbundles $u \in \{p, q, s\}$ (colors) as a function of the relative subbundle sizes Ξ_p for different ratios of Ξ_q/Ξ_s (titles). The continuous line shows values computed with the variational approach and the crosses illustrate the corresponding results of the vertex model assuming arcs of constant curvature. For large subbundle sizes, deviations between the two models become visible (e.g. green graph and crosses in the rightmost plot $\Xi_q/\Xi_s = 10$).

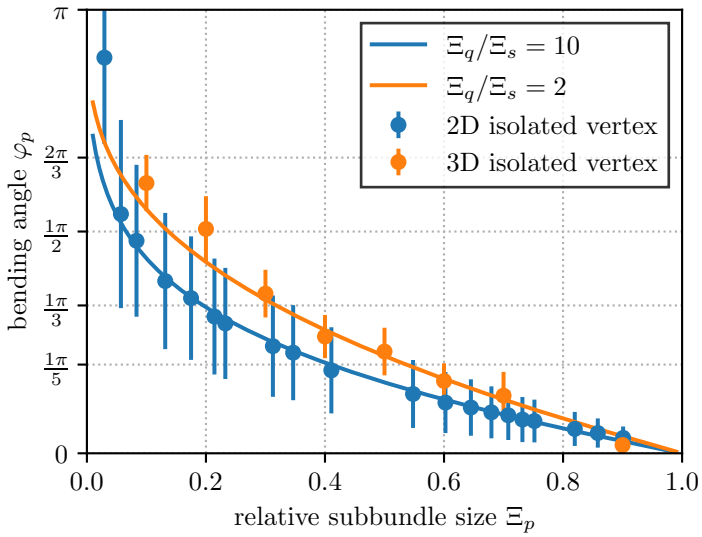

FIG. S13. Numerically determined angles of minimal energy (lines) for different subbundle size ratios Ξ_q/Ξ_s in circular arc approximation. Isolated vertex simulations (2D for $\Xi_q/\Xi_s = 10$, 3D for $\Xi_q/\Xi_s = 2$) are performed to assess the model predictions. Errorbars indicate one standard deviation.

V. NETWORK STRUCTURE DURING COARSENING

In this section, we show additional results on the network structure during coarsening regarding the area and shape, and the mesh angles at vertices, the polymers per bundle, the neighbor distribution (Aboav-Weaire law), and the Lewis- and Feltham laws.

A. Distribution of mesh shapes

We characterize mesh shapes in the network of bundled polymers by the two eigenvalues λ_1 and λ_2 of the area moment of inertia tensor $I_{ij} = \int_{\text{mesh}} \mathrm{d}a\, x_i x_j$. For each mesh, we determine an equivalent ellipse matching the eigenvalues of the area moment of inertia tensor, see also Fig. S8 c). An ellipse with semi-major and semi-minor axes $R_{\max}$ and $R_{\min}$ has $\lambda_1 = (\pi/4) R_{\max}^3 R_{\min}$ and $\lambda_2 = (\pi/4) R_{\max} R_{\min}^3$. During coarsening of the network the

distribution of the anisotropy ratio $R_{\min}/R_{\max}$ characterizing mesh shapes is invariant with a maximum around $R_{\min}/R_{\max} = \sqrt{\lambda_2/\lambda_1} \approx 0.7$, see Fig. S14. This supports the existence of an invariant scaling state of the network of bundles during coarsening. The stable anisotropy distribution seems compatible with experimental results for circular chambers in Ref. [11].

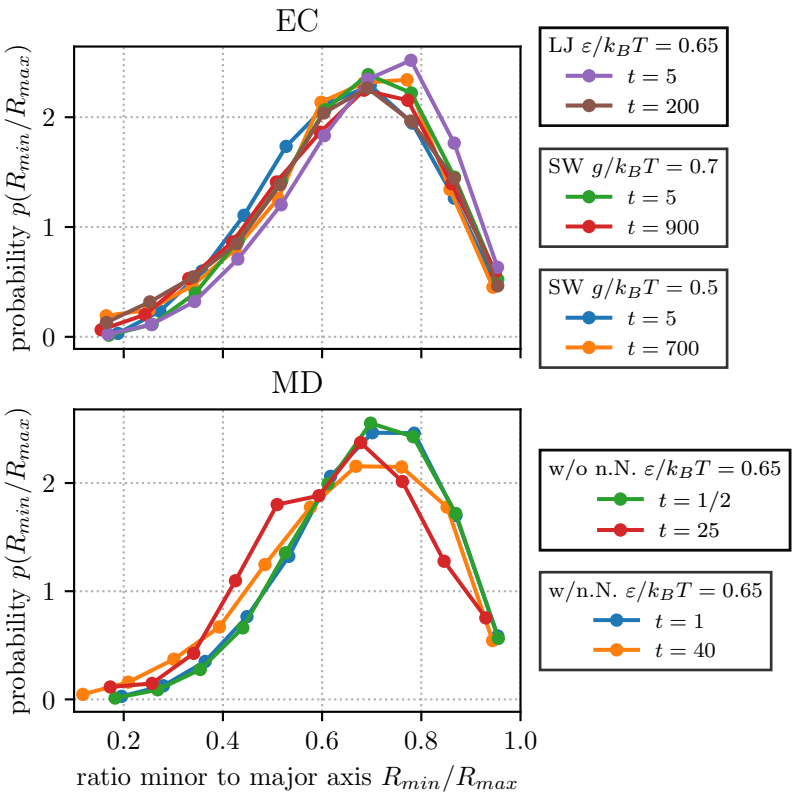

FIG. S14. Histograms of the mesh anisotropies $R_{\min}/R_{\max}$ defined as the ratio of the semi-minor to the semi-major axis of equivalent ellipses (see Fig. S8). The upper and lower figure show results for ECMC and MD simulations, respectively. Simulation times are given in multiples of 10^4 Sweeps (ECMC) or $10^6\,\Delta t$ (MD). All histograms exhibit very similar shapes indicating that the mesh anisotropy distribution is invariant during the ongoing coarsening process of the network.

B. Polymers per bundle (bundle width)

Fig. S15 shows that the average number of polymers per bundle (or bundle width) $\langle N_p \rangle$ grows during coarsening, while the distribution of the relative number of polymers per bundle $N_p/\langle N_p \rangle$ over the network remains invariant. This supports the existence of an invariant scaling state of the network of bundles during coarsening.

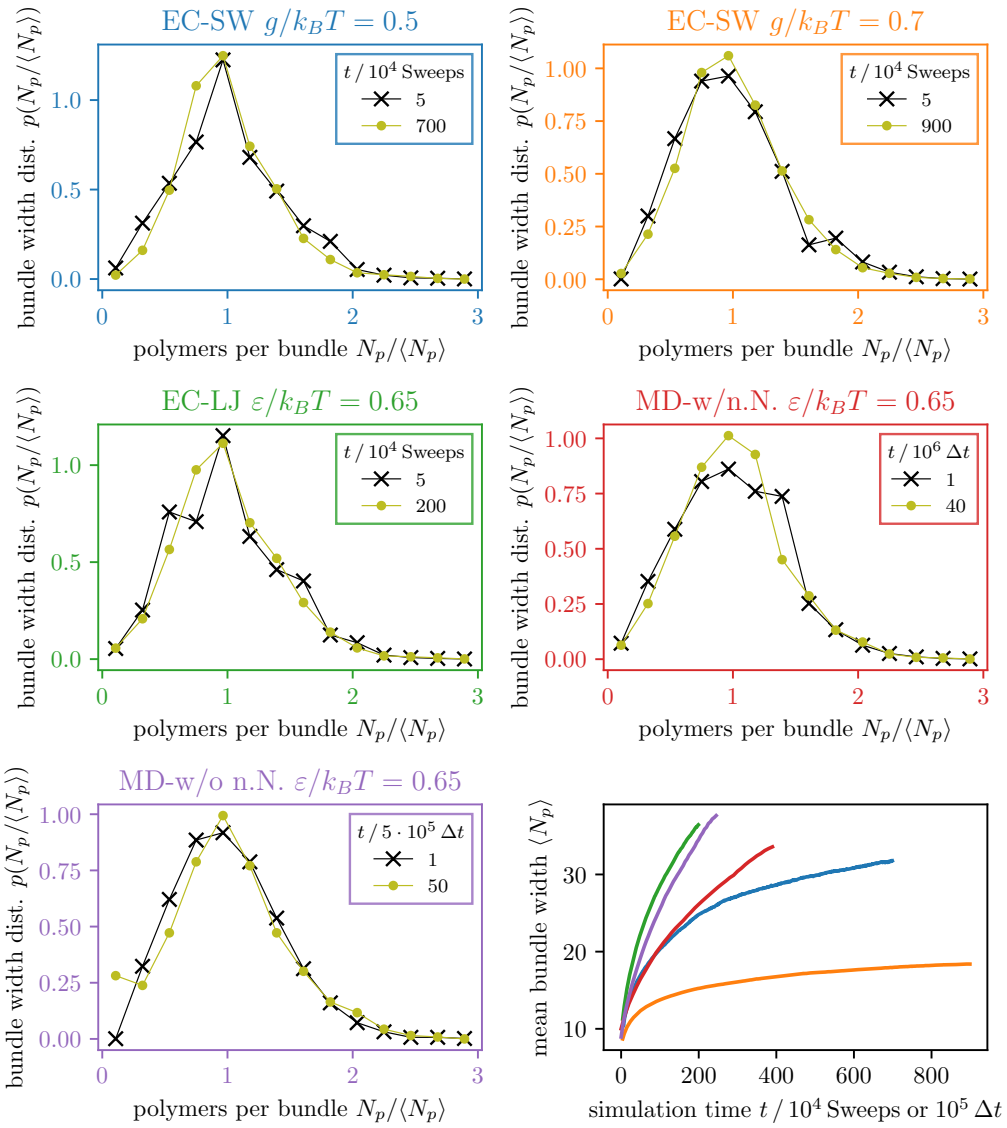

FIG. S15. Histograms of the relative number of polymers per bundle $N_p/\langle N_p \rangle$ for different pair interactions and simulation types at early (black) and late (green) simulation times. The histogram markers are connected by lines as a guide to the eye. The figure in the lower right corner shows the evolution of the mean number of polymers per bundle $\langle N_p \rangle$ as function of the simulation times t. The color of the graphs therein matches to the color assigned to the respective figure title and frame, i.e. simulation type. A plot of the relative variance $\mathrm{var}(N_p/\langle N_p \rangle)$ as a function of the simulation time is shown in Fig. S19.

C. Mesh angles

Fig. S16 shows additional simulation data for mesh angles. In the main text we present data for ECMC simulations with square well potentials (EC-SW) and attraction $g = 0.7\,k_BT$; here, we show data for $g = 0.5\,k_BT$, data for ECMC simulations with LJ-attraction (EC-LJ) and data for MD simulations with disabled LJ-interactions for bonded beads (MD-w/o n.N.) and including all LJ-interactions (MD-w/n.N.). Comparing different simulations as well as different simulation times t, we find the distributions of the mesh angles and the mean values after binning to be similar and largely invariant during coarsening. This supports the existence of an invariant scaling state of the network of bundles during coarsening.

The mean bending angles computed after binning the data with respect to Ξ_p (black dots) are described very well by a relation linear in Ξ_p (black dashed line). Our model predictions (blue line) are similarly close for all but very small subbundles $\Xi_p \leq 0.1$. This suggests that effects of the surrounding network structure become increasingly important in the limit of small subbundles, where the network prevents the complete folding of the small subbundle p to $\varphi_p = \pi$ if the two larger subbundles essentially zip together (see Fig. S9c).

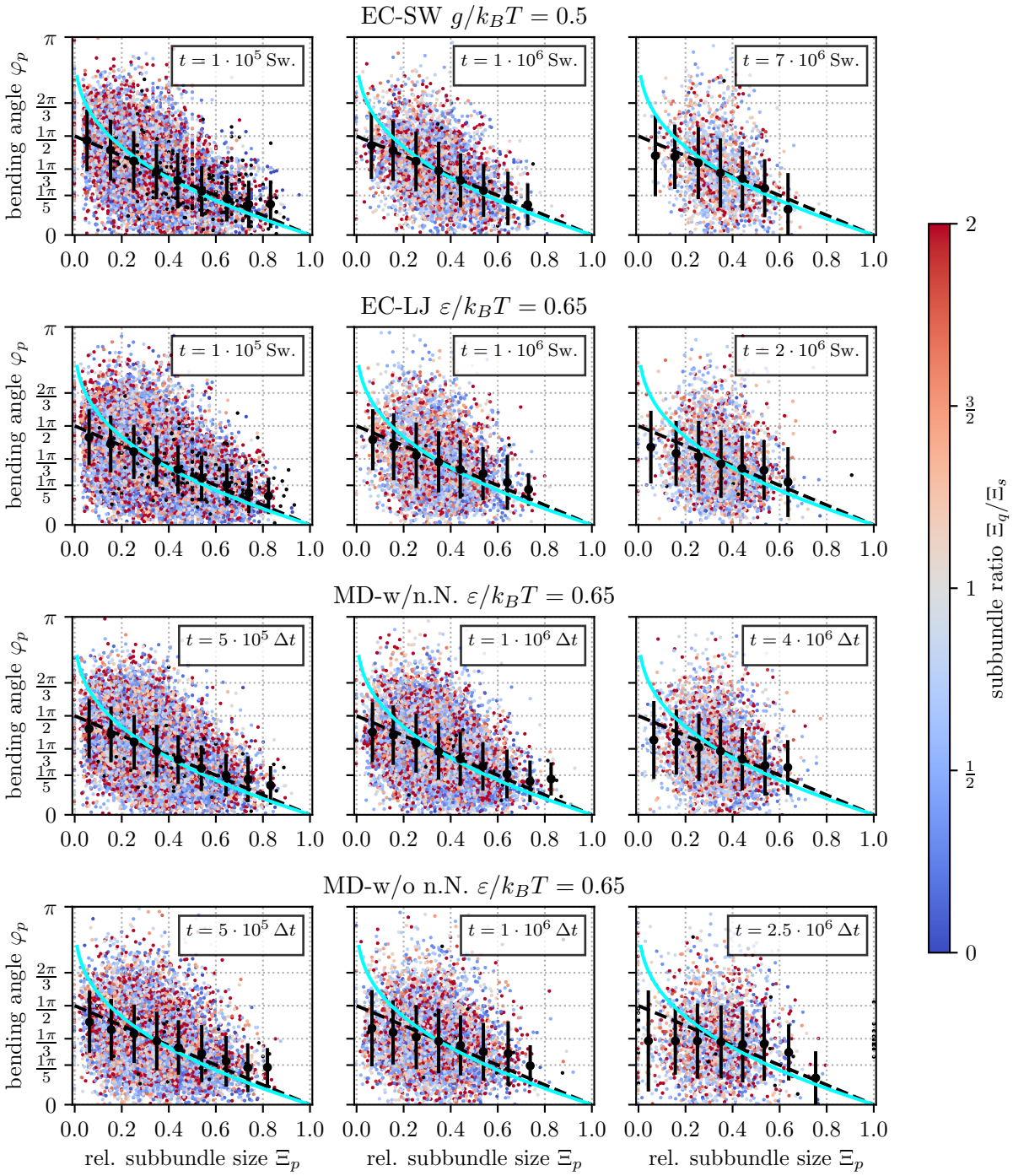

FIG. S16. Mesh angles measured from network simulations for simulation sets excluded from the main text. As before, the cyan graph shows the vertex model prediction ($\Xi_q = \Xi_s$) and the dashed line is the linear relation $(1 - \Xi_p)\pi/2$. All plots exhibit a similar scattering of the angles compared to the plots in the main text (Fig. 2b) albeit the dots in the plots are not equally dense in consequence of the different levels of coarsening reached at the respective simulation time t specified in the legend. Surprisingly, the mean values of φ_p (black dots) obtained from MD-w/o n.N. at late simulation times (lower right corner) seem to lean more towards Plateaus law $\varphi_p = \pi/3$ instead of the linear expression (dashed line) or the model prediction. We assume this effect to be due to poor statistics caused by the progressed coarsening and concomitant reduction of the number of vertices in these systems. Indeed, performing the same analysis at earlier simulation times yields results in line with the other analyzed simulations.

D. Aboav-Weaire law and neighbor distribution

A gamma distribution with probability density function

$$P(n) = \frac{\lambda^\alpha}{\Gamma(\alpha)} n^{\alpha-1} \exp(-\lambda n)$$

is the starting point for the (continuous) approximation of the distribution of the number of neighbors. Given the logic of our image analysis procedure, the smallest possible number of neighbors of a mesh is three and we renormalize the density to take the smaller support $n \in [3, \infty)$ instead of $n \in (0, \infty)$ into account. The density function $P(n)$ remains virtually unchanged except for the gamma function $\Gamma(\alpha)$ which has to be replaced by the upper incomplete gamma function $\Gamma(\alpha, 3)$.

The distribution of the number of neighbors must fulfill the condition $\langle n \rangle = 6$ to be compatible with Euler's theorem. We use this additional constraint to fix the rate parameter λ as a function of the shape parameters α and effectively obtain a one-parameter distribution. The first moment of the renormalized distribution reads

$$\langle n \rangle = \frac{\alpha}{\lambda} + \frac{\lambda^{\alpha-1}}{\Gamma(\alpha, 3)} 3^\alpha \exp(-3\lambda) \stackrel{!}{=} 6 \; .$$

This equation cannot be solved analytically for $\lambda(\alpha)$ but we employ a numerical root finding algorithm to compute the rate parameter λ. Therefore, the procedure of estimating the parameters of maximum likelihood (MLE) for $p(n)$ given the sample of edge numbers becomes a one-dimensional non-linear optimization problem. The resulting curves are shown in Fig. 2 of the main text or in Fig. S17 below.

Fig. S17 shows additional simulation data for the Aboav-Weaire relation $m(n)$ and probability $P(n)$ of finding a mesh with n edges. In the main text we present data for ECMC simulations with square well potentials (EC-SW) and attraction $g = 0.7\, k_B T$; here, we show data for $g = 0.5\, k_B T$, data for ECMC simulations with LJ-attraction (EC-LJ) and data for MD simulations with disabled LJ-interactions for bonded beads (MD-w/o n.N.) and including all LJ-interactions (MD-w/n.N.). We find similar distributions for all simulations. With increasing simulation time (right column in Fig. S17), we observe a gradual widening of the of the distribution, i.e. meshes with a small number of edges ($n = 3$) and large numbers of edges $n > 10$ become more frequent. The increasing value of the edge number variance μ_2 obtained from the Aboav-Weaire fit as well as direct computation (see Fig. S19) is consistent with this observation.

For the formulation of a relation between the mean bundle length $\langle L_B \rangle$ and the circumference $\langle U \rangle$ (see Sec. VIII below), we also have to compute the first inverse moment of the distribution leading to

$$\left\langle \frac{1}{n} \right\rangle = \frac{\lambda^\alpha}{\Gamma(\alpha, 3)} \int_3^\infty \mathrm{d}n \, \frac{1}{n} n^{\alpha-1} \exp(-\alpha n) = \frac{\lambda}{\alpha - 1} \left(1 - \frac{\lambda^{\alpha-1}}{\Gamma(\alpha, 3)} 3^{\alpha-1} \exp(-3\lambda) \right) \; , \tag{8}$$

where we have assumed $\alpha > 1$ consistent with the parameters found from fitting the density to the histograms.

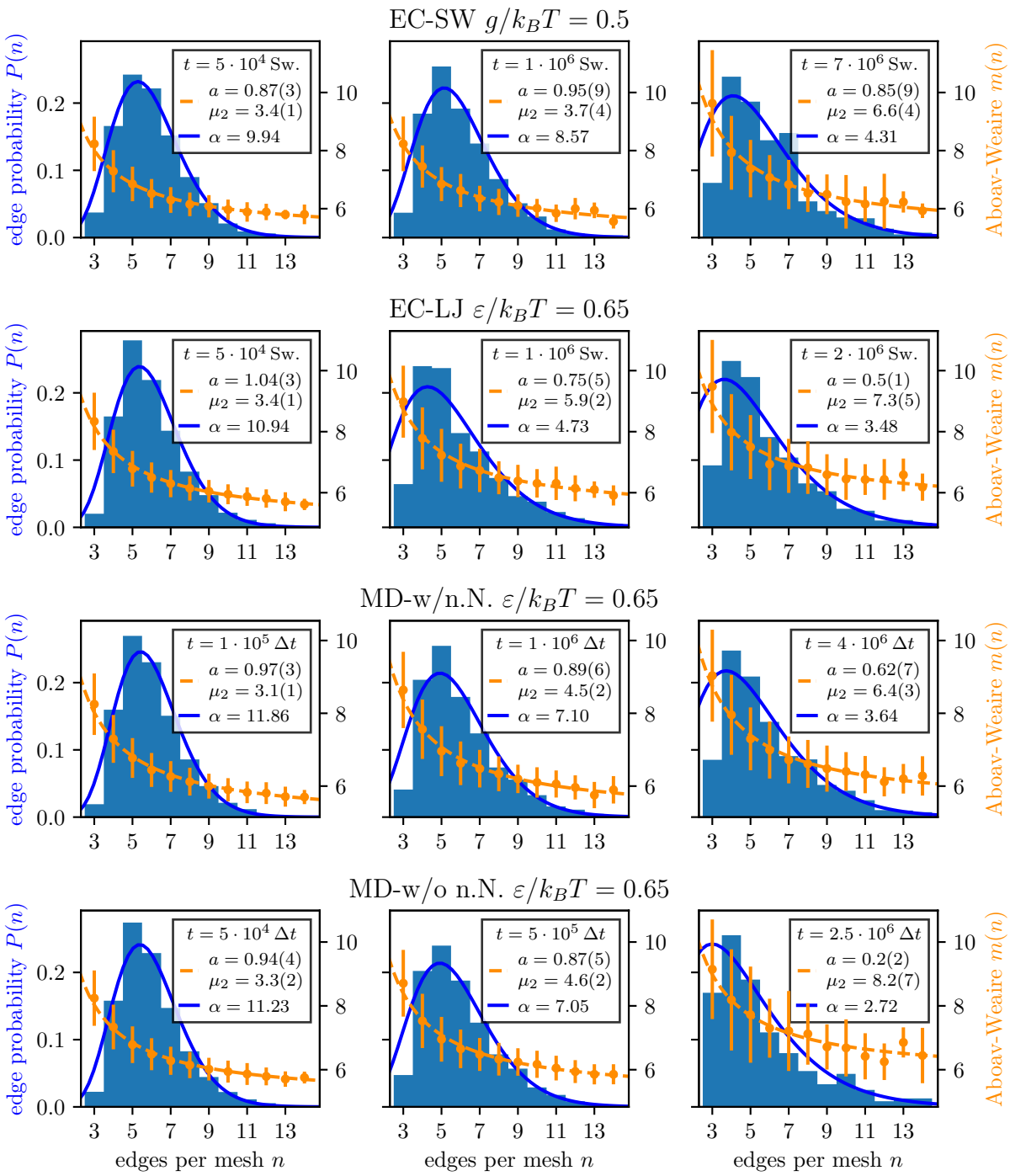

FIG. S17. Aboav-Weaire relation $m(n)$ (orange) and probability $P(n)$ of finding a mesh with n edges (blue) for simulation sets omitted from the main text. The same functions $m(n) = 6 - a + (6a + \mu_2)/n$ and $P(n) = \lambda^\alpha(\Gamma(\alpha, 3))^{-1} n^{\alpha-1} \exp(-\lambda n)\Delta n$ are used for the fitting or MLE procedure. While the qualitative resemblance to the results presented in the main text remains, we find larger deviations from the Aboav-Weaire law in particular for simulations with LJ pair-interactions at large simulation times t. The computed fit parameter a is no longer close to the theoretically expected value $a = 1$ albeit still of the same order of magnitude. For the set of simulations with disabled pair-interactions among directly bonded beads (MD-w/o n.N.), the large uncertainties on the fit parameters can be attributed in part to poor statistics because the coarsening process has already reduced the number of meshes in the system considerably.

E. Lewis- and Feltham-laws

Fig. S18 shows additional simulation data to Lewis- and Feltham-laws. In the main text we present data for ECMC simulations with square well potentials (EC-SW) and attraction $g = 0.7\,k_BT$; here, we show data for $g = 0.5\,k_BT$, data for ECMC simulations with LJ-attraction (EC-LJ) and data for MD simulations with disabled LJ-interactions for bonded beads (MD-w/o n.N.) and including all LJ-interactions (MD-w/n.N.). We find similar results for all simulations at different simulation times t supporting the existence of an invariant scaling state.

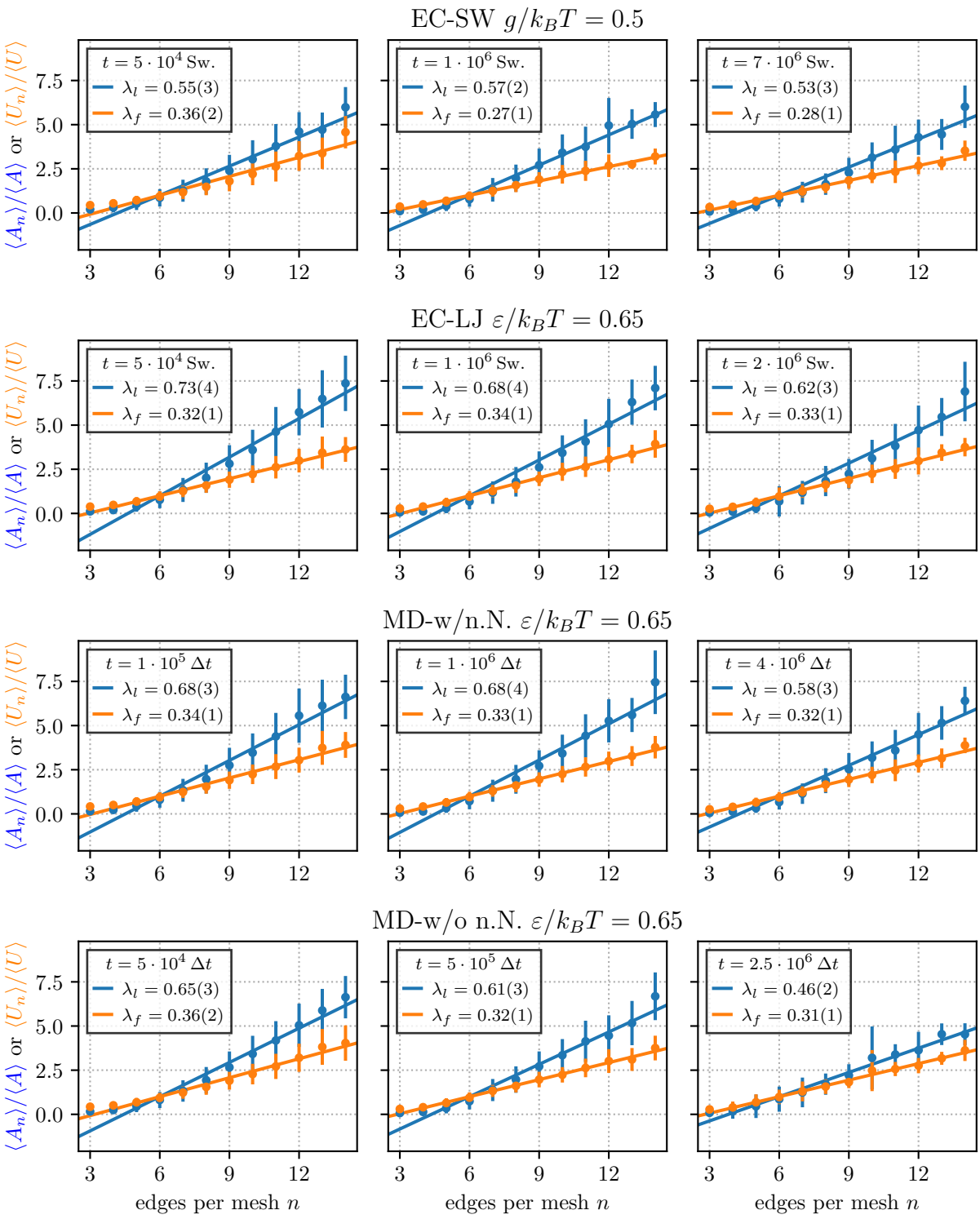

FIG. S18. Comparison of simulation data to Lewis- and Feltham-laws $\langle f_n \rangle / \langle f \rangle = \lambda_i (n - \langle n \rangle) + 1$ for simulations not included in the main text. We denote the mean area and circumference of the set of meshes with n edges as $\langle A_n \rangle$ and $\langle U_n \rangle$, respectively. The parameters λ_i are computed from a fitting procedure against the simulation data. Errorbars represent one standard deviation. All simulations show very similar behaviour. The best agreement with Lewis-law is observed for MD simulations with disabled pair interactions for bonded beads (MD-w/o n.N.) at late simulation times t.

F. Variances of polymers per bundle and number of neighbors

One hallmark of a state of statistical self-similarity is a constant variance of the number of neighbors n. The measured increase of var(n) is consistent with visually apparent widening of the histograms in Fig. S17 contradicting a strict scaling state. On the contrary, the variance of the relative number of polymers per bundle var($N_p/\langle N_p\rangle$) exhibits only minor variations in agreement with the histograms in Fig. S15 and supporting the existence of a scaling state.

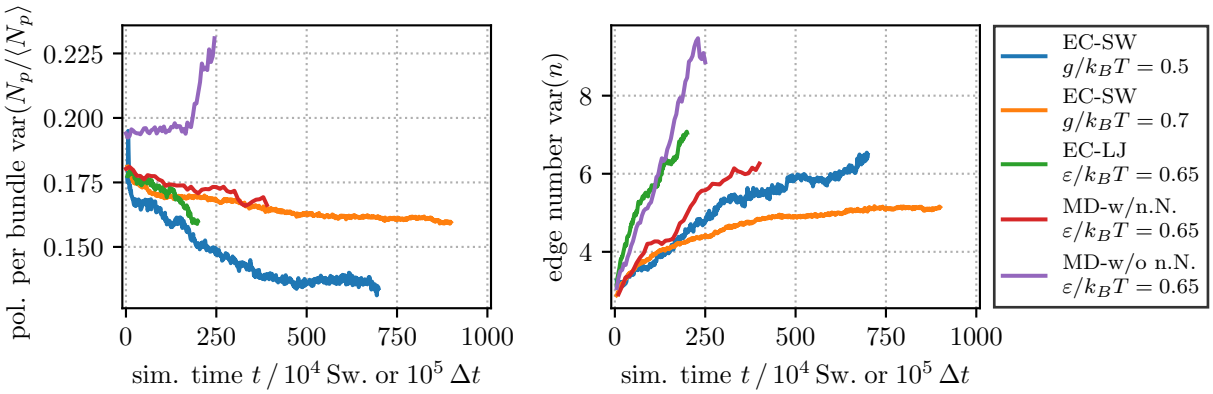

FIG. S19. Variance of the relative number of polymers per bundle var($N_p/\langle N_p\rangle$) (left) and variance of the edge-number distributions $P(n)$ (right) shown in Fig. S15 and S17 as a function of the simulation time. With exception of the ECMC simulations at $g/k_BT = 0.7$, the simulation data shows no sign of a plateau in var(n). For the interpretation of the asymptotically constant variance observed for the EC-SW $g/k_BT = 0.7$, we recall the tendency of these systems to evolve towards kinetically trapped states. Consequently, the constant (or very slowly increasing) value of var(n) should be ascribed to the slow dynamics of the system instead of a state of statistical self-similarity. The variance of the relative number of polymers per bundle var($N_p/\langle N_p\rangle$) exhibits only minor variations.

G. Mesh area distribution and variance

During coarsening the average mesh area A grows. The distribution of the relative area $A/\langle A\rangle$ and its variance, on the other hand, should remain invariant in a self-similar scaling state during coarsening. However, the results in Fig. S20 show a widening trend of the mesh area distribution (and a corresponding increase in its variance) for all pair interactions and simulation types contradicting the existence of a strict scaling state.

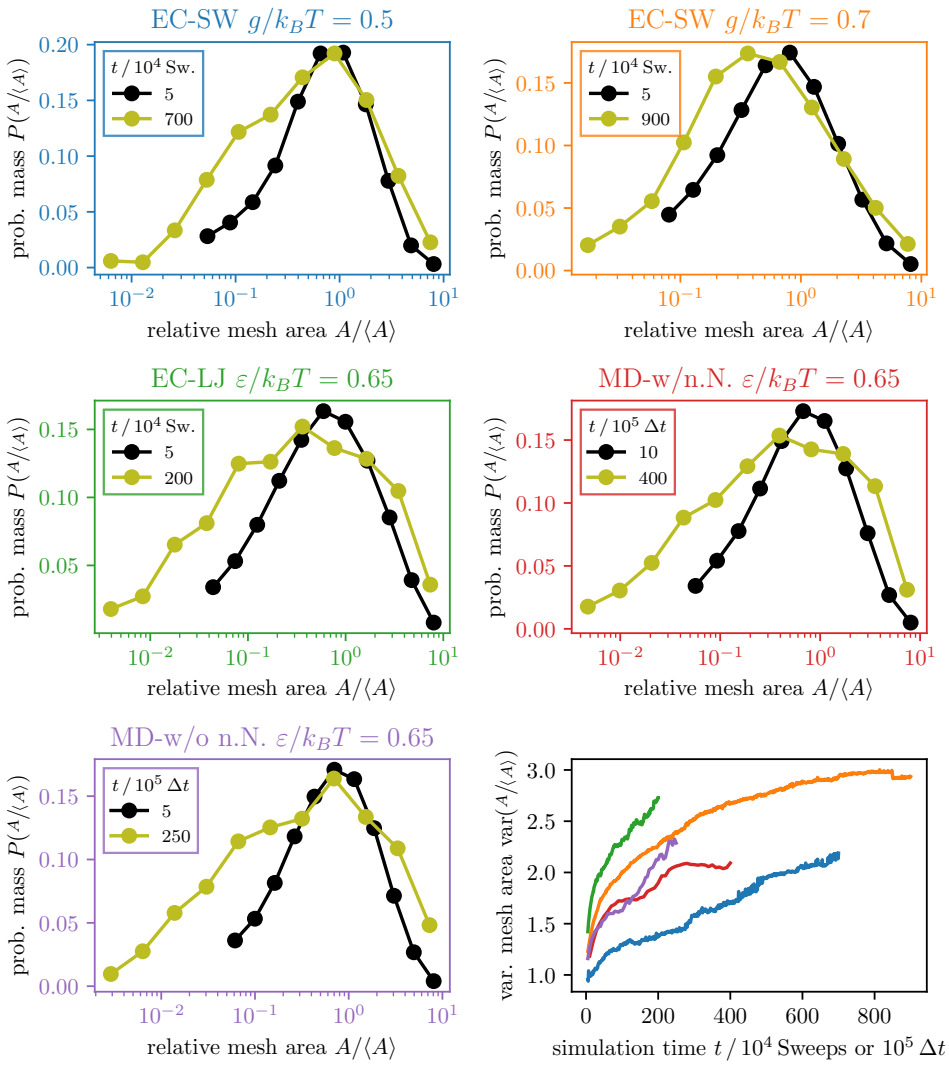

FIG. S20. Probability mass functions (histogram weights times bin width) of the relative area $A/\langle A\rangle$ measured at early (black) and late (green) simulation times for different pair interactions and simulation types. Even for early simulation times, the histograms indicate the occurrence of very inhomogeneous mesh areas (note the log-scale on the $A/\langle A\rangle$-axis). All different sets of simulations show the same trend towards further widening of the distribution. This observation is confirmed by the plot at the bottom right corner showing a steady increase of the variance var$(A/\langle A\rangle)$ as a function of the simulation time.

VI. COALESCENCE OF MESHES BY RUPTURE

One coarsening mechanism is bundle rupture. It occurs either at the center of a bundle as shown in Fig. 2e in the main text but may also occur at a branching point of the network as shown in Fig. S21.

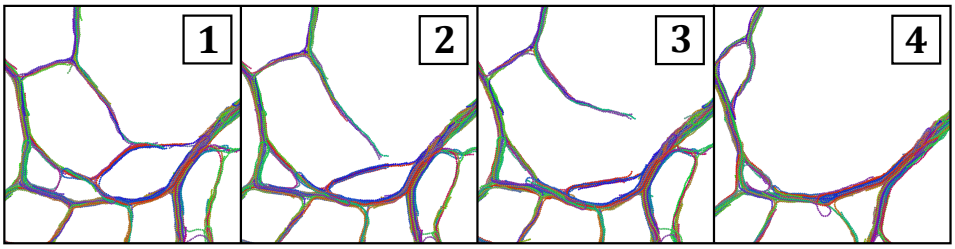

FIG. S21. Alternative version of a rupture process during network coarsening. The applied polymer model does not allow for a rupture of polymer chains. If one or several polymers traverse the entire bundle from vertex to vertex, the rupture process illustrated in Fig. 2e) can be suppressed. Instead, the tension due to the network effects a desorption of two bundles at the vertex. Again, this process involves sliding of the persistent bundle during the relaxation.

VII. SUPPRESSION OF COARSENING BY STIFF SPRINGS, STIFF OR LONG POLYMERS AND CRYSTALLIZATION

The coarsening dynamics depends on details of nearest neighbor interactions, which influence the process of polymer sliding. Coarsening effectively stops in a kinetic arrest in the presence of very stiff springs, similar to spring constants used in Ref. [12] ($k \approx 30\,000\, k_B T/\sigma^2$ as opposed to $k = 100\, k_B T/\sigma^2$ in our simulations) as shown in Fig. S22. Therefore, the coarsening observed in our simulations does not contradict the quenched structures reported in Ref. [12] but rather highlights the importance of the bead-bead interaction along the polymer for the network dynamics.

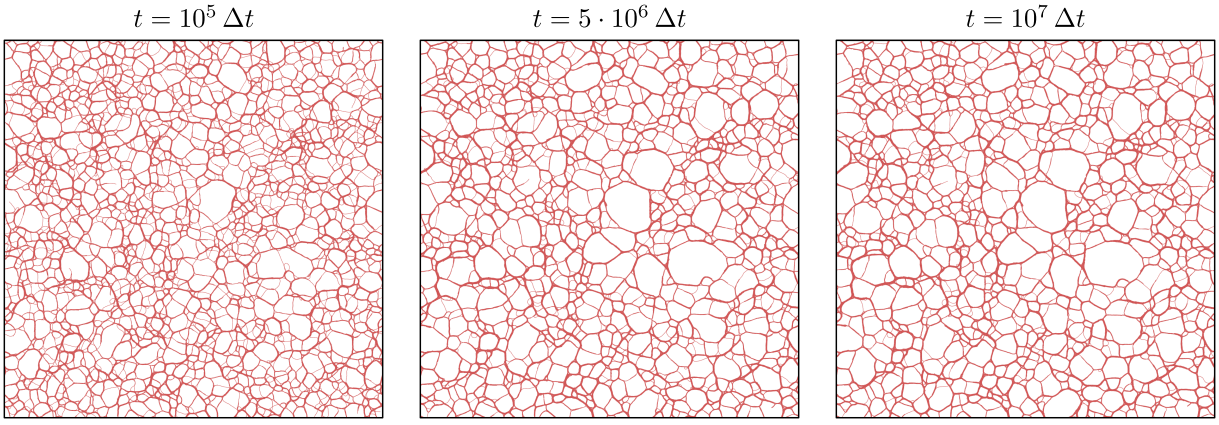

FIG. S22. Snapshots of an MD simulation performed with parameters similar to Ref. [12] ($k \approx 30\,000\, k_B T/\sigma^2$, $\varepsilon \approx 1.7\, k_B T$, $\kappa \approx 100\, k_B T\sigma$ in our unit system). The large spring constant (compared to $k = 100\, k_B T/\sigma^2$ used in the coarsening simulations) suppresses the coarsening process.

In a similar manner, the coarsening process can be impeded by very stiff polymers, i.e. polymers with large persistence length. In systems of mutually attractive polymers within this parameter regime, the suppression of the coarsening process has been attributed to stabilizing triangular features at the vertices of the bundle network in Refs. [7, 8]. For stiffer polymers, zipping processes that require "u-turns" of polymers within a bigger subbundle are suppressed. We can reproduce this observation in our simulations by increasing the bending stiffness from $\kappa = 30\, k_B T\sigma$ to $\kappa = 1000\, k_B T\sigma$ (see Fig. S23). However, unlike the results presented in the references, coarsening is not entirely prevented in our simulations - likely because of the presence of ripping processes (if polymers are not very long in addition) and because of the influence of thermal activation in our system compared to the athermal behaviour reported in Refs. [7, 8].

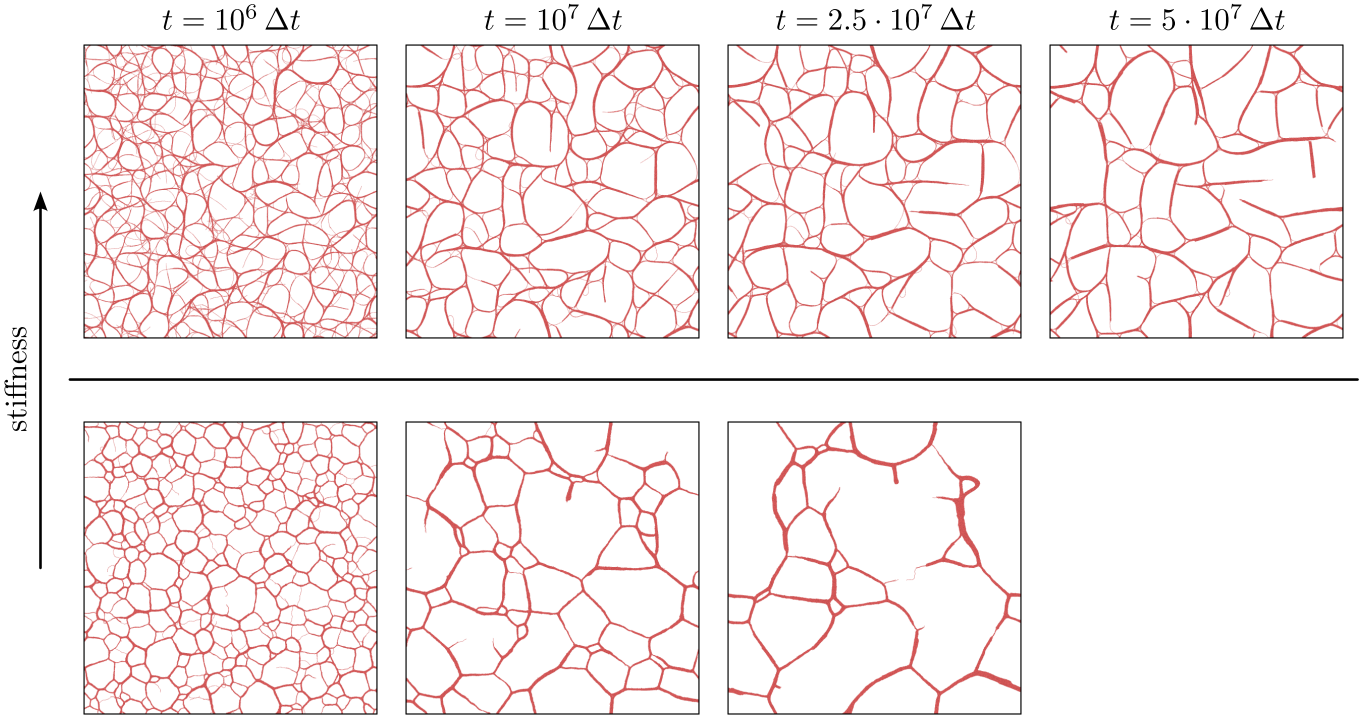

FIG. S23. Comparison of the coarsening dynamics of bundled polymer networks with very stiff polymers (top, $\kappa = 1000\,k_BT\sigma$) to those with lower bending stiffness used in our simulations (bottom, $\kappa = 30\,k_BT\sigma$). The columns display simulation snapshots at different simulation times. While coarsening can be observed in both systems, it proceeds significantly faster with more flexible polymers (bottom).

Coarsening is also impeded for longer polymers (keeping the total particle density in the simulation constant). The increased length of the polymers suppresses ripping processes of bundles and, thereby, one coarsening mode of the network structure. In Fig. S24 we present a time series of snapshots with polymers comprising of $N_b = 200, 400$ beads as compared to $N_b = 100$ used thus far. A visual inspection of the snapshots reveals that the emerging cellular structure is not very sensitive with respect to the length of the individual polymers. However, the coarsening dynamics is significantly slowed down with increasing polymer length and we no longer find any dangling bundles as a transient leftover due to a ripping event. Compared to the results reported in Refs. [7, 8], the coarsening process is not entirely prevented because of the lower bending stiffness used in our simulations. Therefore, zipping processes continue to be possible and are, in fact, the dominant coarsening mode.

Accordingly, we find the coarsening process to become very slow for long and stiff polymers. A time series of snapshots for such a system is shown in Fig. S25. While some coarsening can be observed at early simulation times, the dynamics slow down as ripping and zipping processes are suppressed and the thermally activated dissociation of entire subbundles against the attractive potential becomes improbable for bundles with more than just a few polymers.

In the DPD (Dissipative Particle Dynamics) simulation approach in Ref. [13], where semiflexible polymers are composed of sticky elastic beads, a similar coarsening regime has been identified, which arrests by crystallization of the attractive beads themselves. These simulations were performed at much higher potential strengths corresponding to $g/k_BT \sim 2$, while we work at weak binding $g/k_BT \lesssim 1$ in our simulations. Our attractive potential strengths remain far below the crystallization transition of the attractive bead fluid, e.g. the critical temperature for Lennard-Jones systems is $k_BT_c/\varepsilon \approx 1.1$ [14] whereas we have $k_BT/\varepsilon = 1/0.65 \approx 1.5$. In our simulations, the association of polymers into bundles is solely due to their polymeric nature: attractive beads are connected to polymers, which enhances the attraction between polymers and gives rise to bundle formation. The set of parameters we use for our simulations is therefore more similar to the 'liquid networks' briefly discussed in Ref. [13]. In agreement with our simulations, a prolonged coarsening is reported and bundle merging as well as polymer reptation are identified as coarsening mechanisms; processes that we called zipping and rupture.

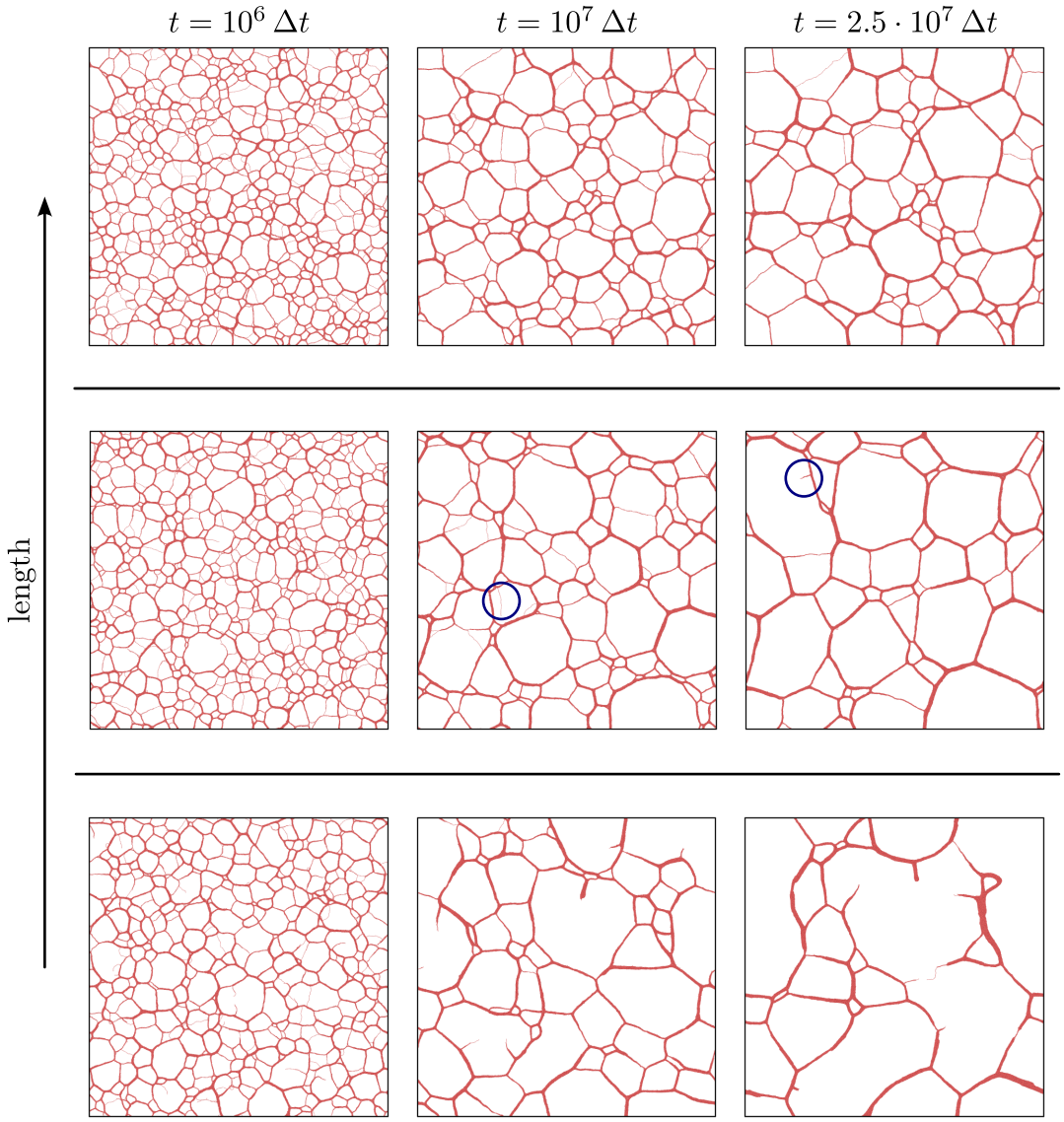

FIG. S24. Comparison of the coarsening dynamics of bundled polymer networks assembled from polymers of different lengths (top: 400 beads per polymer, center: 200 beads, bottom: 100 beads) while keeping the total particle density in the simulation volume constant. The columns display simulation snapshots at different simulation times. Coarsening of the mesh structure is found irrespective of the polymer length. However, the coarsening proceeds considerably slower for longer polymers. A closer inspection of the presented snapshots reveals that the increased polymer length suppresses ripping processes: the transient occurrence of dangling bundles is most frequent for shorter polymers (bottom) and becomes very rare with increasing polymer length (blue circles, center) until virtually all ripping events of bundles are suppressed (top).

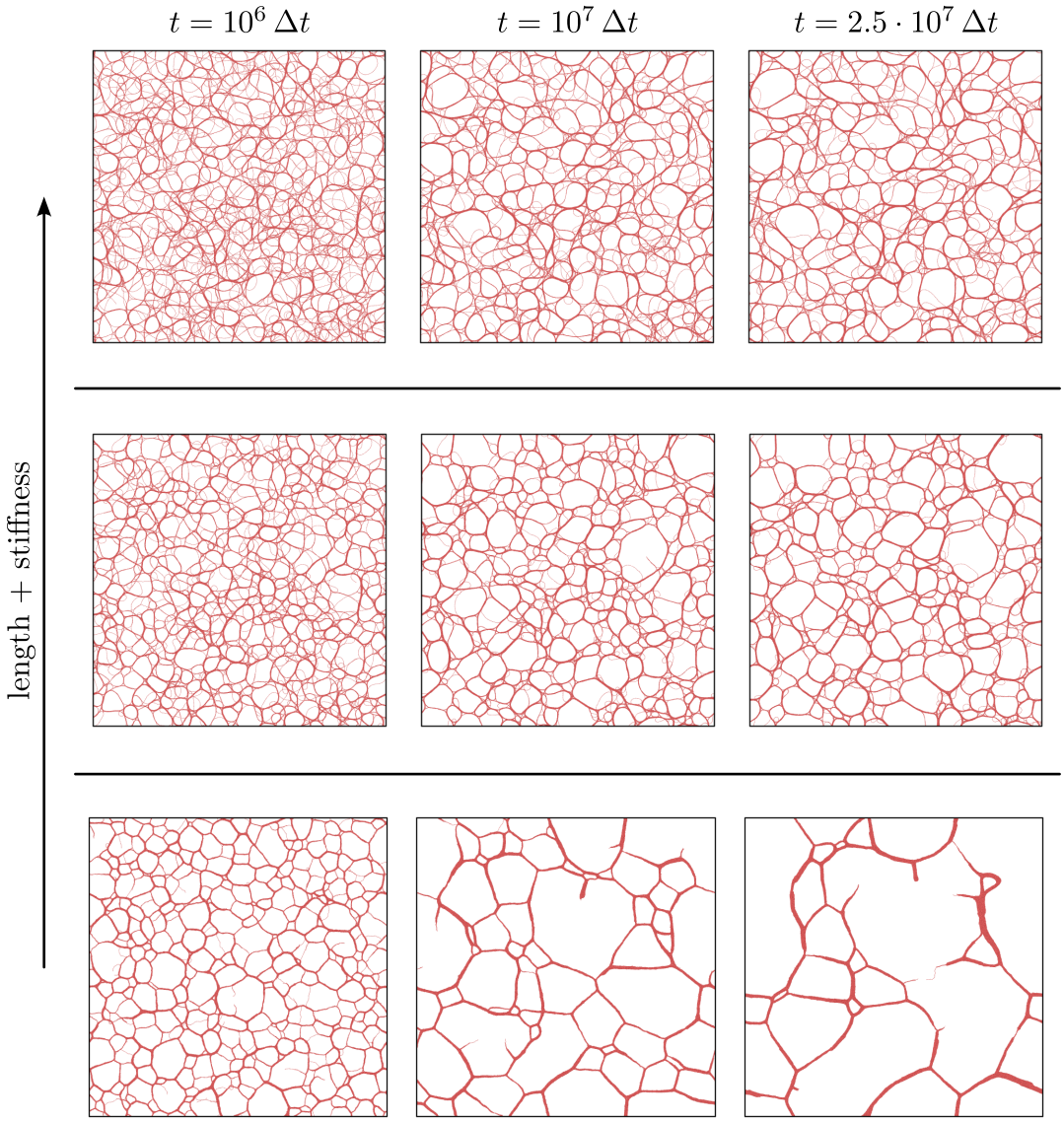

FIG. S25. Time series of snapshots from an MD simulation of long (400 beads) and stiff (top: $\kappa = 1000\,k_BT\sigma$, center: $\kappa = 300\,k_BT\sigma$) polymers compared to the previously used parameters (bottom: 100 beads, $\kappa = 30\,k_BT\sigma$). The overall particle density in the simulation volume is identical to the other simulations. Compared to the other simulations snapshots shown in this section, we find not only a significantly slower coarsening but also the frequent occurrence of single or two polymer loops inside larger meshes. The occurrence of such loops becomes more frequent with increasing κ. In Fig. S23 and Fig. S24, such loops are dissolved either by zipping (introducing a "u-turn") or dissociation of one polymer end (i.e. a rupture of the bundle due to the finite polymer length).

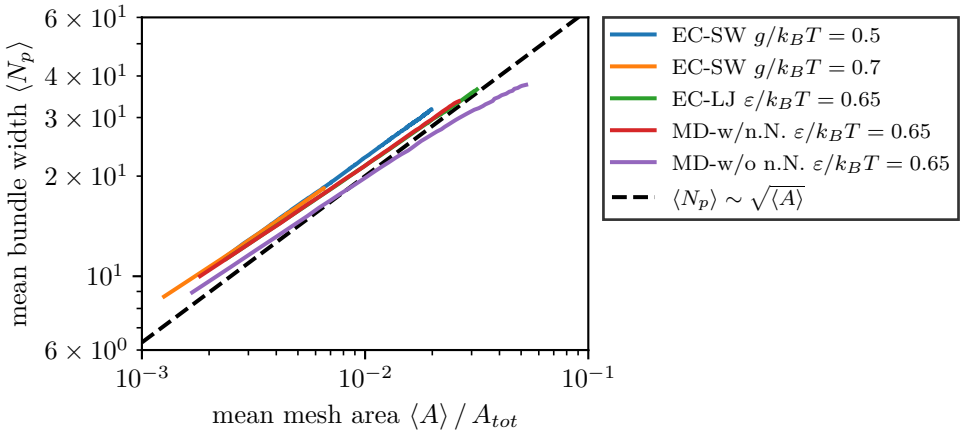

FIG. S26. Predicted scaling of the mean number of polymers per bundle (bundle width) $\langle N_p \rangle$ with the mean mesh area $\langle A \rangle$ compared to measurements form network simulations. The dashed black line represents the theoretical prediction.

VIII. SCALING LAWS OF NETWORK PROPERTIES

Based on the structural properties of the bundle network, we can derive several scaling laws relating bundle properties relevant to the coarsening dynamics such as the mean bundle length and mean tensile force per bundle to structural properties such as the mean mesh area $\langle A \rangle$. These scaling laws will hold during coarsening and govern the dynamics of coarsening.

The scaling laws are based on the approximate conservation of total length of polymer in the system, $N_{poly} L_{poly} = L \approx \text{const}$. Assuming an even distribution of L to all edges, the mean number of polymers per bundle becomes

$$\langle N_p \rangle = \frac{2L}{N_m \langle U \rangle} \sim \frac{2L}{A_{tot}} \langle A \rangle^{1/2} \,,$$

where $\langle U \rangle \sim \langle A \rangle^{1/2}$ denotes the mean circumference and $N_m \approx A_{tot}/\langle A \rangle$ the number of meshes in the network ($A_{tot} = L_x L_y$ is the fixed total area of the system). The scaling prediction $\langle N_p \rangle \propto \langle A \rangle^{1/2}$ can be tested against measurements from network simulations. Fig. S26 shows a good agreement between theory and simulation albeit the exponent of the scaling is slightly overestimated. The deviation from the power law increases for large $\langle A \rangle$.

The mean bundle length, i.e. edge length, can be computed from the edge number distribution (renormalized gamma distribution) used for fitting the histograms in Fig. S17

$$\begin{aligned}
\langle L_B \rangle &= \sum_n P(n) \langle L_n \rangle \\
&= \sum_n P(n) \frac{\langle U_n \rangle}{n} \\
&\approx \sum_n \left(\lambda_f P(n) + \frac{1 - \lambda_f \langle n \rangle}{n} P(n) \right) \langle U \rangle \,,
\end{aligned}$$

where $\langle L_n \rangle$ and $\langle U_n \rangle$ are mean bundle length and mean circumference of all meshes with n edges. In the last line we assume Felthams law $\langle U_n \rangle / \langle U \rangle = \lambda_f (n - \langle n \rangle) + 1$ to be an adequate approximation. Applying a continuity approximation and using the relation (8) of the gamma distribution, the sum yields

$$\langle L_B \rangle = \langle U \rangle \left(\lambda_f + \frac{(1 - \lambda_f \langle n \rangle)\lambda}{\alpha - 1} \left[1 - \frac{\lambda^{\alpha-1}}{\Gamma(\alpha, 3)} 3^{\alpha-1} \exp(-3\lambda) \right] \right) \equiv B(\lambda_f, \alpha) \langle U \rangle \,.$$

This implies the scaling

$$\langle L_B \rangle \sim B \langle U \rangle \sim B \langle A \rangle^{1/2} \sim (B A_{tot}/L) \langle N_p \rangle.$$

A scaling prediction of the mean force $\langle F \rangle$ along each bundle is motivated from the change in the total binding energy with respect to the mean bundle length. The total energy due to the beads short ranged pair interaction can

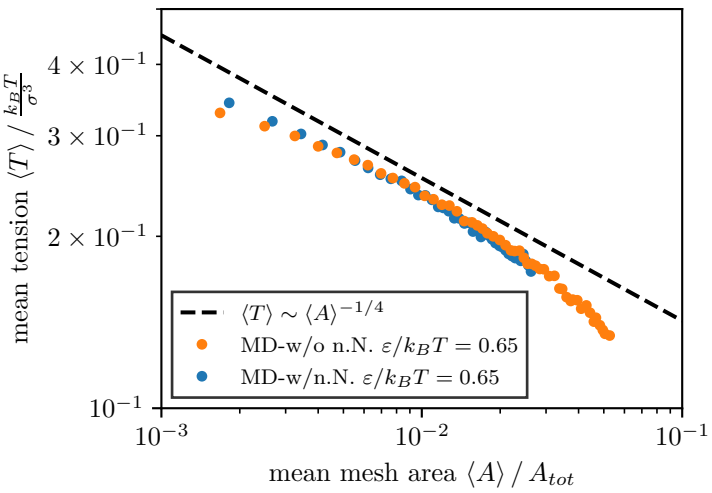

FIG. S27. Double-logarithmic plot of the mean tension vector $\langle T\rangle \sim \langle F\rangle/\langle N_p\rangle$ measured in MD simulations as a function of the mean mesh area $\langle A\rangle$. The dashed black line visualizes our scaling prediction $\langle T\rangle \sim \langle A\rangle^{-1/4}$.

be approximated by

$$E_p = \frac{N_m\langle U\rangle}{2}\left(\tilde{a}\langle N_p\rangle - \tilde{b}\sqrt{\langle N_p\rangle}\right) \sim L\left(\tilde{a} - \tilde{b}\langle N_p\rangle^{-1/2}\right) . \tag{9}$$

The first factor $N_m\langle U\rangle/2 \sim L\langle N_p\rangle^{-1} \sim A_{tot}\langle A\rangle^{-1/2}$ on the right hand side of the equation corresponds to the total bundle length of the network, the second factor describes the energy per bundle length. Its first term $\propto \langle N_p\rangle$ represents the bulk and the second term the surface contributions. A similar expression for the adhesion energy per bundle length was proposed by Sengab and Picu [7, 8]. The system aims to decrease its energy by reducing the surface term, that is forming less bundles of broader width. These arguments motivate

$$\langle F_{tot}\rangle \sim \frac{\partial E_p}{\partial\langle L_B\rangle} \sim \frac{\partial E_p}{\partial\langle N_p\rangle}\frac{\partial\langle N_p\rangle}{\partial\langle L_B\rangle} \sim \frac{L^2\tilde{b}}{BA_{tot}}\langle N_p\rangle^{-3/2} \propto \langle A\rangle^{-3/4} ,$$

where we used the initial assumption $L \approx$ const. The mean force per bundle becomes

$$\langle F\rangle \sim \frac{\langle F_{tot}\rangle}{N_m} \propto \langle A\rangle^{1/4} .$$

To test this prediction against simulation data, we have to measure the stress tensor for each bundle in the network. We therefore couple the MD simulations to the image analysis procedure to assign beads to edges (see Sec. IIIc) and measure the stress tensor in short simulation runs as the average over the stresses on all particles in the respective bundle. The norm of the stress vector T is computed from the stress tensor times the normalized vector along the edge direction. Given $\langle F\rangle \sim \langle N_p\rangle\langle T\rangle \sim$ bundle width $\times$ tension, we find the scaling prediction $\langle T\rangle \sim \langle A\rangle^{-1/4}$, which is largely confirmed in Fig. S27.

The deviations from our scaling prediction are likely due to contributions from the springs and the bending stiffness to the stress tensor, whereas the energy expression (9) motivating the scaling of the force takes only the pair interaction of the beads into account. Even though we have measured the stress tensor only in MD simulations, we expect a similar scaling for the Square Well pair potential simulations (EC-SW) because our scaling arguments do not depend on details of the interactions but only assume some kind of short ranged attractive interaction.

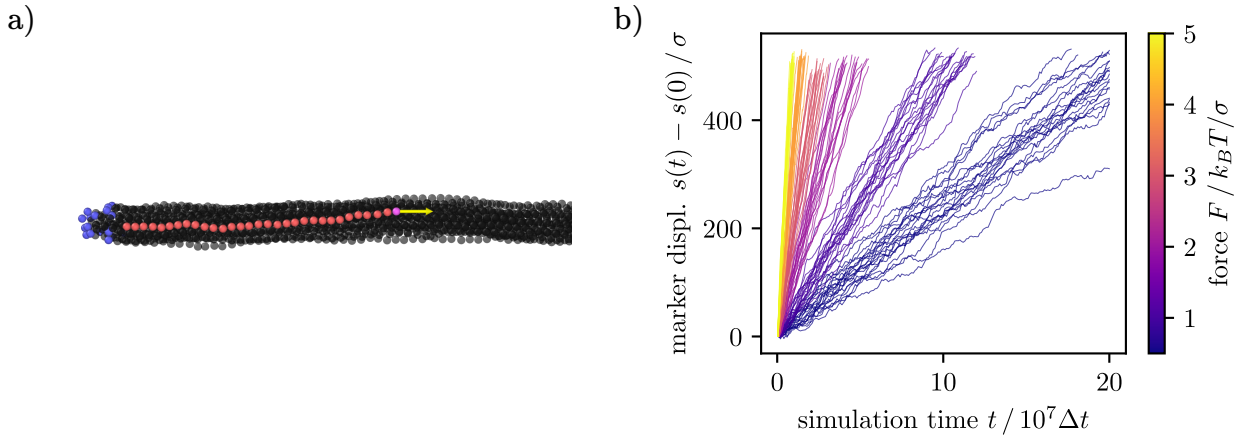

FIG. S28. Simulations of polymer bundles for the measurement of the effective friction constant. a) Configuration of a bundle simulation as described in the text. The marker polymer (red) is dragged along the reference bundle (gray) by an external force (yellow arrow) acting on the marker end bead (purple). The end beads of the reference bundle (blue) are fixed on one side. b) Displacement s of the marker bead as a function of time for different forces F in the range from $0.5\,k_BT/\sigma$ to $5\,k_BT/\sigma$ and a marker polymer of $N_{marker} = 40$ beads. We performed 20 simulations for each force.

IX. POLYMER FRICTION

Coarsening dynamics is governed by the processes of bundle zipping and bundle rupture. Both in bundle zipping and bundle rupture polymers have to slide through a bundle, which is hindered by friction. Therefore, it is essential to characterize polymer friction in order to derive analytical results for the coarsening dynamics.

To investigate the friction law caused by the interactions of different polymers in a bundle, we perform MD simulations of long polymer bundles fixed at one end (*reference bundle*) with an additional polymer of shorter length (*marker polymer*), that is subject to a one-sided external force F pulling the marker along the bundle (see Fig. S28a). We generate the initial configurations of the polymer bundle by randomly placing all polymers (including the marker polymer) in a straight conformation around the bundle axis with a random (3d) offset proportional to the square root of the number of polymers in the bundle. Therefore, the marker is not always in the middle of the bundle at the start of a simulation. The force F is only applied at the end of the marker polymer to mimic a tension-induced force from a vertex. We will consider different lengths of marker polymers by changing the number N_{marker} of beads; the reference bundle will always be sufficiently long to enclose the marker polymer over its entire length. We consider different marker polymer lengths because in bundle zipping and bundle rupture the sliding polymer length $N_{marker} \propto L_B$ depends on the typical bundle length L_B of the network. The reference bundle consists of at least 20 polymers. The simulations apply the same set of interaction parameters as the MD simulations of the bundled networks, in particular an LJ energy scale $\varepsilon = 0.65\,k_BT$ and the spring constant $k = 100\,k_BT/\sigma^2$ unless specified otherwise.

From these simulations, we can measure the marker polymers displacement along the reference bundle as a function of time and the set of simulation parameters. This gives access to the friction law $v = v(F)$ for the sliding velocity of the marker polymer as a function of pulling force. Since we aim to describe the network coarsening process, we are mainly concerned with the parameter dependencies of the friction that change during the simulation, i.e. the length of the bundles (corresponding to the marker length N_{marker}), the pulling force F, and the number of polymers in the surrounding reference bundle.

A. Viscous or solid friction

The mean velocity of the displacement is computed as the linear fit $s(t) - s(0) = vt$. To distinguish between viscous friction and solid-like friction, we perform a series of simulations with different values of F applied to the marker. For viscous friction, we expect $v \approx F/\gamma$ and consequently $s(t) \propto F$. As opposed to this flow behavior for viscous friction, we take thermal activation over energy barriers as hallmark of solid-like friction. Thermal activation results in a non-linear scaling of v with the applied force, e.g. the Tomlinson model $v \sim \sinh(CF)$ for thermally activated barrier crossing [15], where $C = \Delta x/k_BT$ is related to the typical distance Δx between energy barriers.

The simulation results in Fig. S29 strongly indicate a solid-like friction for all marker lengths ($N_{marker} = 20 - 100$ beads) and the measurements can be accurately fitted with the Tomlinson model prediction. Indeed, solid-like friction

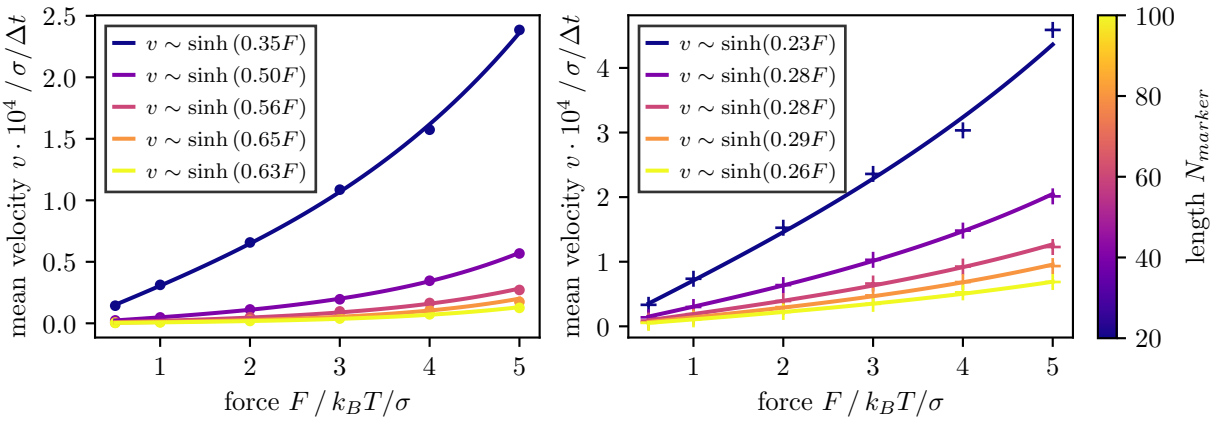

FIG. S29. Mean velocities as a function of the applied external force F for five different lengths of the marker polymers $N_{marker} = 20$, 40, 60, 80, 100 beads. Here, v is averaged over all simulations for each force. The function $B\sinh(CF)$ is fitted to the data. Left: LJ pair interactions are taken into account between all beads along a polymer. Right: Pair interactions are disabled for first, second and third nearest neighbors along a polymer.

has also been found in *in-vitro* studies of sliding actin filaments [16]. In our model, neighboring bead-spring polymers tend to "lock in" [17], which requires thermal activation for sliding. This suggests that also details of nearest neighbor interactions along a polymer are important for polymer sliding, because absence of nearest neighbor interaction can allow the polymer to deform more easily for thermal activation to the next locked state.

To investigate the role of thermal activation on the marker displacement further, we performed simulations of bundles at low temperature $T_1 = T/10$ as well as simulations with a constant energy integrator plus an explicit viscous damping. Either way, the depletion of kinetic energy results in stalling of the marker polymer and, even for the largest external force considered here, no marker displacement is observed on the simulation timescale emphasizing the relevance of thermal activation for the sliding process. The fitting results $CK_BT/\sigma = \mathcal{O}(1)$ suggest that thermal activation proceeds by activation of polymer segments over regularly spaced energy barriers with separation $\mathcal{O}(\sigma)$ and height $\gg k_BT$. The finding that C is largely independent of the length N_{marker} of the marker polymer indicates that the energy barrier spacing is independent of N_{marker}.

B. Marker length dependence of sliding velocity

Next, we turn to the marker length dependence of the velocity. If motion proceeds by thermal activation of polymer segments of finite size (independent of N_{marker}) we expect that the friction constant is proportional to N_{marker} and the sliding velocity $v \sim N_{marker}^{-1}$ if we pull only at the end of the polymer. If the driving forces acts on all beads, we would expect a sliding velocity independent of N_{marker}. If the length of polymer segments participating in thermal activation is larger than or comparable to the marker length, we expect a more pronounced decrease of sliding velocity as a function of marker length.

It is instructive to compare the polymer sliding along the discrete bead structure presented by the other polymers in the bundle with a Frenkel-Kontorova model [16]. In the standard Frenkel-Kontorova model the external driving force acts on all N beads and a sliding velocity independent of N is predicted by thermal activation of kink-like excitations [16]. However, we apply the external force only to the first bead of the marker. We therefore simulated a Frenkel-Kontorova model with Langevin dynamics (FKL) and an external force acting on one particle at the chain end. Our simulations do not reveal any asymptotic plateau region of the center of mass velocity v_{cm} with respect to the chain length N and, instead, we find $v_{cm} \sim N^{-1}$ provided that the magnitude of the external force suffices to effect any chain displacement during the simulated time. This agrees with the proposed dependence of the sliding velocity on N_{marker} for the marker polymer.

Alternatively, the polymers of the reference bundle could be considered as "fixed obstacles", and the marker polymer follows a kind of reptation process. Then, the polymer mobility scales as $\mu \sim N_{marker}^{-2}$ from a diffusive motion of reptating segments [18]. Assuming that this mobility also governs the biased reptation if the polymer is pulled at one end, we find a more pronounced decrease $v \sim N_{marker}^{-2}$.

Fig. S29 already indicates, that the the polymer velocity is decreasing with increasing N_{marker} (at fixed force F). This means that the polymer sliding velocity will also depend on the polymer or bundle length for typical polymer

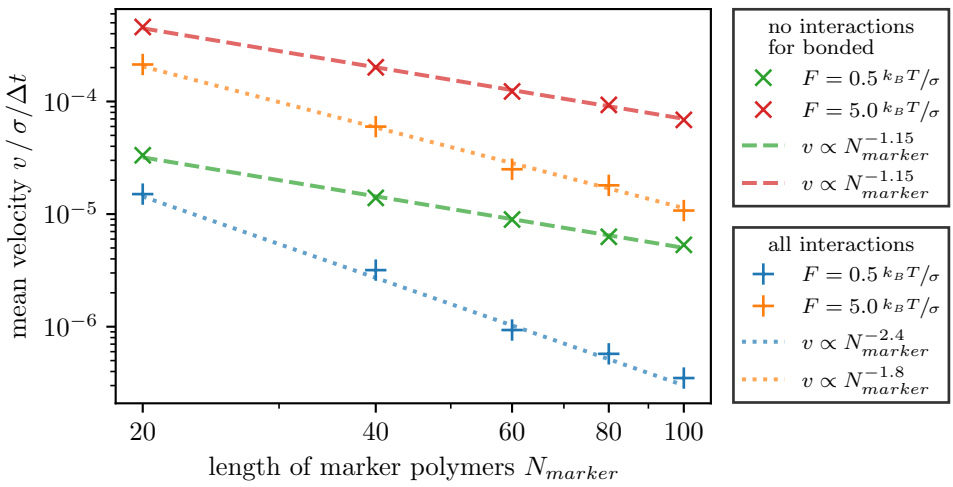

FIG. S30. Double logarithmic plot of the mean velocities as a function of the length of the marker polymers. The external force is set to $F = 0.5\,k_BT/\sigma$ or $F = 5\,k_BT/\sigma$ (see legend). Each marker represents the mean of at twenty simulations. Phenomenologically motivated power-laws are drawn to approximate the scaling. We find different exponents in the power-law if the LJ-interaction is turned off among bonded beads.

lengths in our network simulations (100 beads per polymer). To substantiate this observation, we plot the measured mean velocities against the marker lengths N_{marker} in Fig. S30 for the largest and smallest external force applied in the bundle simulation.

The velocities decrease following a power-law behaviour with respect to the marker length N_{marker} in the interval considered here and accordingly there is no sign of an asymptotic plateau independent of N_{marker}. We also find that the exponent in the power-law can in general depend on the magnitude of the force. According to our above discussion the observed power-law exponents smaller than -1 are plausible. Exponents only slightly smaller than -1 hint to thermal activation of finite polymer segments (independent of N_{marker}) during sliding and the absence of reptating motion.

C. Effect of pair interactions on polymer sliding

Thus far, the simulations included LJ pair interactions between all beads irrespective of bonding topology. The coarsening behaviour of the networks indicates, however, that the sliding dynamics of the polymers is affected from disabling the pair interactions among bonded beads (see Fig. 2f in the main text). Therefore, we perform another set of simulations with disabled LJ interaction for first, second and third neighbors along the polymer chains. The results in Fig. S29 (right) confirm an accelerated sliding of polymers with disabled pair interaction among neighboring beads. Obviously, absence of nearest neighbor interactions allows the polymer to deform more easily and assists thermal activation to the next favorable state. The previously used function $B\sinh(CF)$ still allows a good fit to the data albeit the obtained parameters differ. Similarly, the observed length dependence of the velocity shows power-law behaviour while the exponent differs (see Fig. S30). A qualitative difference can be observed for the scaling of the exponent with respect to F. If the LJ-interaction is turned off for bonded neighbors, the exponent in the power-law becomes independent of F whereas the exponent changes with F when these interactions for bonded beads are included (see Fig. S30). The fit parameter $C = \Delta x/k_BT$ related to the typical distance Δx between energy barriers is slightly smaller in the absence of nearest neighbor interactions. The parameter C becomes independent of N_{marker} in the absence of nearest neighbor interactions.

D. Scaling laws of polymer sliding

The formulation of a scaling relation for the velocity as a function of the force and N_{marker} is further complicated by the fact, that both parameters of the fit shown in Fig. S29 seem to depend on N_{marker} if all pair interactions of beads are included. Interestingly, the parameter C becomes independent of N_{marker} after disabling LJ-interactions for bonded beads. Given the basic assumption of thermally activated barrier hopping in a tilted periodic potential

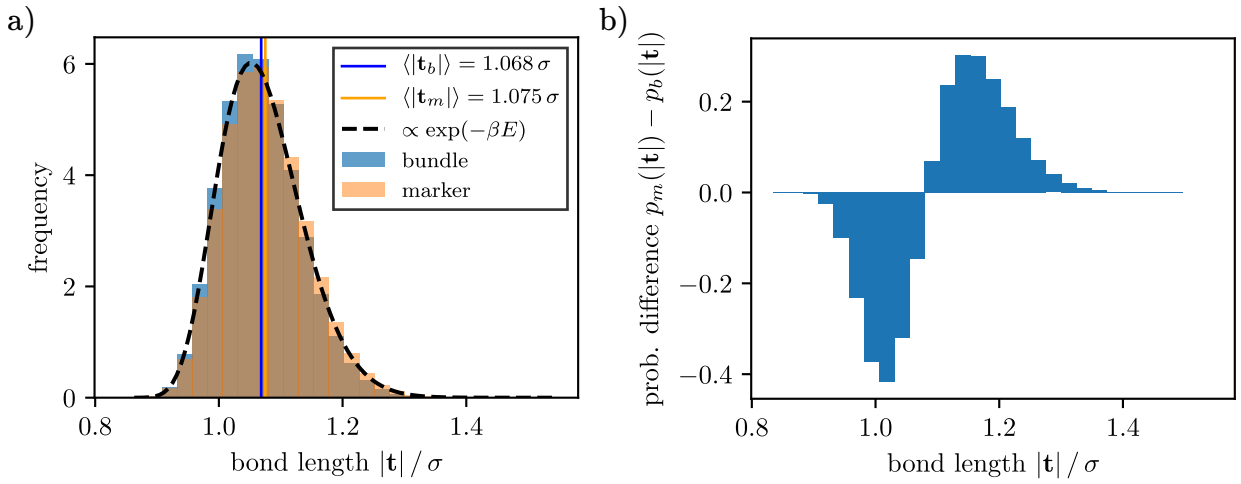

FIG. S31. a): Comparison of a normalised histogram of the bond length $|\mathbf{t}|$ for marker and bundle polymers to the thermal distribution. The marker consists of $N_{marker} = 40$ beads and the external driving force is set to $F = 5\,k_BT/\sigma$. The energy in the thermal Boltzmann distribution consists of the spring energy and a Lennard-Jones contribution of adjacent beads $E(|\mathbf{t}|) = E_{spring}(|\mathbf{t}|) + V_{lj}(|\mathbf{t}|)$. b): Difference of the histogram weights of marker and bundle polymers revealing the slight tendency of bonds in the marker polymer to higher bond lengths.

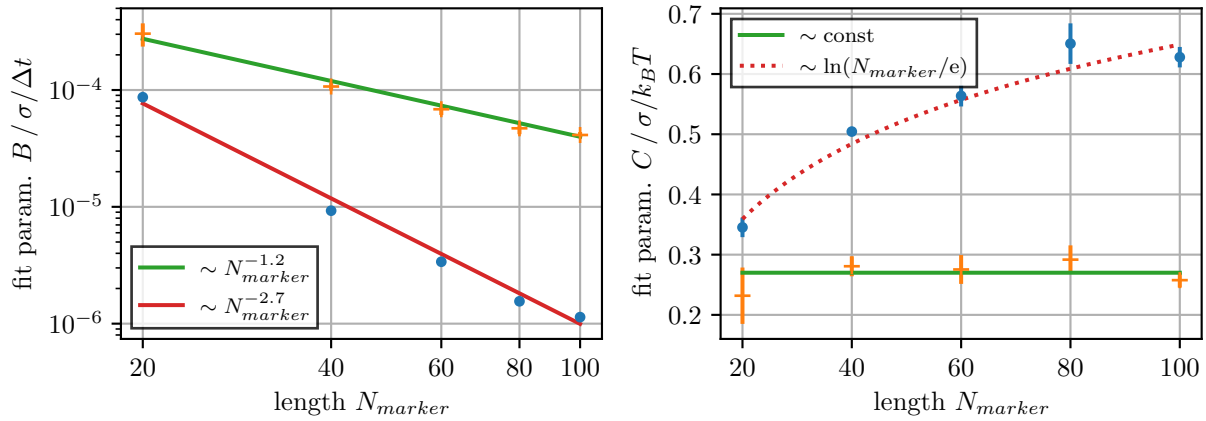

FIG. S32. Fit parameters B and C computed for the simulation data shown in Fig. S29 as a function of the marker polymer length N_{marker}. Dots represent results for simulations which include all Lennard-Jones interactions and pluses show results with disabled LJ interactions for bonded beads. Errorbars (if not smaller than marker size) represent one standard deviation. Power laws are used to approximate the parameter values.

leading to $v \approx B\sinh(CF)$, this effect indicates that the presence (or absence) of pair interactions along the chain modulates the periodicity of the effective potential due to the bundle and/or the force propagation in the chain. In fact, histograms of the bond length show a shift from a symmetric distribution at the spring rest length $\langle|\mathbf{t}|\rangle \approx 1\,\sigma$ to an asymmetric distribution at slightly larger bond lengths $\langle|\mathbf{t}|\rangle \approx 1.07\,\sigma$ corresponding to the minimum of the superposition of spring and Lennard-Jones potential if all pair interactions are included (see Fig. S31).

The periodicity of the effective bundle potential is thus affected by the interactions, but this does not explain the emergence of a length dependence in the parameter C. To move forward, we extract empirical scaling relations for the fit parameters with respect to N_{marker} on the length scales relevant to the network coarsening process (Fig. S32).

As stated previously, the parameter C does not depend on the marker length $C \approx$ const and, correspondingly, the scaling of $B \sim N_{marker}^{-1.1}$ practically agrees with results presented in Fig. S30 if LJ interactions between bonded beads are absent. As soon as LJ interactions are included for bonded beads, the length dependence is "split up" to both parameters with opposing tendencies. The parameter B decreases considerably faster with $N_{marker}^{-2.7}$ compared to the scaling observed in Fig. S30 whereas C increases with the marker length.[19] A logarithmic function provides a slightly better approximation for the scaling of parameter $C \sim \ln(N_{marker}) - 1$ as a function of N_{marker} compared

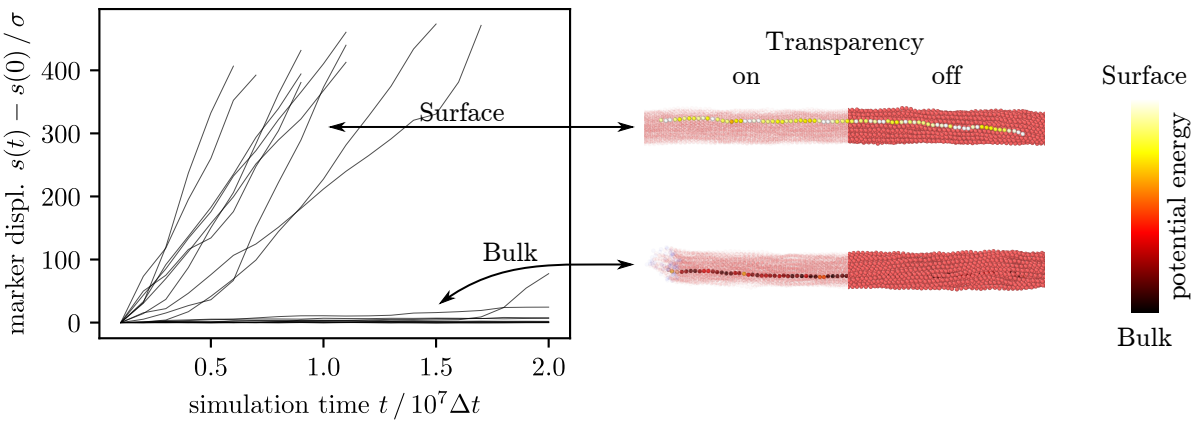

FIG. S33. Simulations with 50 bundle polymers and one marker polymer of length $N_{marker} = 80$ beads. The pulling force is set to $F = 5\, k_B T/\sigma$. Left: If the marker polymer is located on the surface of the bundle, the applied force is sufficient to displace the marker along the bundle. Marker polymers in the interior of the bundle (denoted as *bulk*) show almost no displacement on the simulated timescales. Right: Representative snapshots from two simulation runs. The beads of the marker polymers are colored with respect to the LJ potential energy.

to a simple power law. However, there is no theoretical justification to prefer one ansatz over the other. Overall, we find a scaling of the velocity

$$v \approx B \sinh(CF) \approx BCF \,, \tag{10}$$

where B decreases as a power law with exponents smaller than -1 in N_{marker} and C is either constant or scales logarithmically. The second approximation in the equation holds for small F.

E. Influence of bundle width and microscopic sliding dynamics

The role of the friction gets even more intricate if the width of the reference bundle is increased. As long as the reference bundle does not contain more than approximately 20 polymers, the marker polymer is practically always located on the bundle surface. We find a drastic reduction of the marker mobility up to a point where the marker is almost stalled in simulations of bundles with 50 polymers (see Fig. S33).

Despite the exerted force, hardly any displacement of the markers is measured until there is a transition of the marker from the bulk region to the surface of the bundle. Unlike the isolated bundles considered here, the tension within the bundled network acts on all polymers of a bundle instead of a distinct single one. Therefore, network coarsening will be dominated by the sliding motion of polymers that are located on the bundle surface irrespective of the total bundle width. Furthermore, the histogram in Fig. S15 reveals, that bundles with more than $N_p = 40$ polymers rarely occur and the difference between the effective bulk and surface friction will be neglected in the formulation of the scaling laws.

We also tried to gain some understanding of the microscopic motion of the beads giving rise to the macroscopic sliding of the chain in order to motivate the importance of the interactions between bonded beads. In particular, we are looking for dynamical features qualitatively similar[20] to the Frenkel-Kontorova model, where the translation of the chain typically proceeds via compression or elongation solitons (kinks and anti-kinks) or, in the case of damping and weak driving, an event-based hopping of beads (avalanches) reminiscent of self-organized criticality [21, 22]. However, visual inspection of the dynamics generated by the MD simulations does not reveal any signs of propagating kinks or event-based dynamics in the bundle or the marker polymer. Instead, we find the behaviour of the beads to be dominated by thermal fluctuations. This is confirmed by histograms of the bond length $|\mathbf{t}|$ closely resembling the thermal Boltzmann-distribution. A histogram of the bond length measured exclusively in the marker polymer exhibits a slight tendency towards larger $|\mathbf{t}|$ as a consequence of the pulling force.

An investigation of the load transfer from the marker to the bundle polymers is performed in a similar manner by measurement of a bond length histogram of bonds in direct vicinity of the pulled marker. The deviations from the thermal reference are even smaller indicating that the load transfer is distributed approximately evenly along the marker.

X. DERIVATION OF THE COARSENING RATE

In this section, we derive the coarsening rate of the network of bundles characterized by the change of the mean mesh area $\mathrm{d}\langle A\rangle/\mathrm{d}t = \langle\dot{A}\rangle$ based on the scaling relations presented in the previous sections VIII on structural network properties and IX on polymer friction. Neglecting area coverage caused by the finite width of the bundles, the mean mesh area $\langle A\rangle$ is inversely related to the number of meshes N_m in the system of total area A_{tot}

$$\frac{\langle A\rangle}{A_{tot}} \approx \frac{1}{N_m} \, .$$

The number of meshes changes during the course of the simulation in consequence of ripping and zipping events occurring at rates R_r and R_z, i.e. $\dot{N}_m = -(R_r + R_z)$. We link the change of the mean area to the event rates by computing the derivative

$$\frac{\langle\dot{A}\rangle}{A_{tot}} = -\frac{\langle A\rangle^2}{A_{tot}^2}\dot{N}_m = \frac{\langle A\rangle^2}{A_{tot}^2}\left(R_z + R_r\right) .$$

To close this differential equation in terms of the mean areas, we build upon the scaling arguments of the previous sections. In doing so, we do not distinguish between zipping and ripping even though zipping events are observed more frequently in typical simulations of our systems, because we expect both coarsening modes to exhibit the same scaling. Both processes involve the relative sliding of polymers on the length scale of the bundle lengths L_B. Using the polymer sliding velocity v investigated in the previous section, we define the characteristic event time $\Delta t \sim L_B/v$. From there, we obtain the scaling of the event rates

$$R \sim \frac{N_m}{\Delta t} \sim \frac{N_m v}{L_B} \overset{(10)}{\approx} \frac{N_m}{L_B} B \sinh(CF)$$

with the simplifying assumption that an event may occur at every mesh. The quantities B and C are in general sensitive to the interaction details along the polymers (see Sec. IX), and we recapitulate

$B \sim L_B^{-1.2}$	$C = \text{const}$	for MD-w/o n.N.
$B \sim L_B^{-2.7}$	$C \sim \ln(L_B/\sigma\mathrm{e})$	for MD-w/n.N. and EC-LJ,

where we have identified the length of the moving segment N_{marker} with the mean bundle length L_B in the network. The results of Sec. VIII allow to rewrite all quantities in these equations as functions of the mean mesh area $\langle A\rangle$, namely $N_m \sim \langle A\rangle^{-1}$, $L_B \sim \langle A\rangle^{1/2}$, $F \sim \langle A\rangle^{1/4}$. After power counting and introduction of the abbreviation $a \equiv \langle A\rangle/A_{tot}$, we find

$$\dot{a} = \begin{cases} \hat{b} a^{-1/10} \sinh\left(\hat{c} a^{1/4}\right) \, , & \text{MD-w/o n.N.} \\ \hat{b} a^{-17/20} \sinh\left(\hat{c} \ln\left[\hat{n} a^{1/2}\right] a^{1/4}\right) \, , & \text{MD-w/n.N. and EC-LJ} \end{cases}$$

with two a-independent parameters $\hat{b}$ and $\hat{c}$ (the numerical values used to fit the coarsening simulations are given in Fig. S35). The influence of long and/or stiff polymers on the frequency of zipping and ripping events (see Sec. VII) suggests a dependence of the parameter $\hat{b}$ on polymer length and stiffness because $\hat{b}$ subsumes the proportionality between the event rates and the mean event times as well as the relative frequency of zipping to ripping events. To disentangle the different contributions to $\hat{b}$, an analysis of several sets of simulations with a systematic variation of polymer length and stiffness would be required. The scaling properties of the coarsening dynamics are not affected by these dependencies. To avoid overfitting and simplifying the differential equation, we make the additional assumption $C \approx \text{const}$ for the MD-w/n.N. and EC-LJ systems, given the slow variation of C shown in Fig. S32. This yields the differential equations presented in the main text

$$\dot{a} = \begin{cases} \hat{b} a^{-1/10} \sinh\left(\hat{c} a^{1/4}\right) \, , & \text{MD-w/o n.N.} \\ \hat{b} a^{-17/20} \sinh\left(\hat{c} a^{1/4}\right) \, , & \text{MD-w/n.N. and EC-LJ.} \end{cases} \tag{11}$$

The sinh-function appears as a consequence of the thermally activated polymer motion in the bundle and leads to the breakdown of a pure power law growth of a. This is related to the appearance of the parameter $C = \Delta x/k_B T$ with the typical distance Δx between energy barriers in the argument of the sinh-function; the existence of this additional length scale in thermal activation gives rise to the breakdown of asymptotic power law growth. Only in the limit of

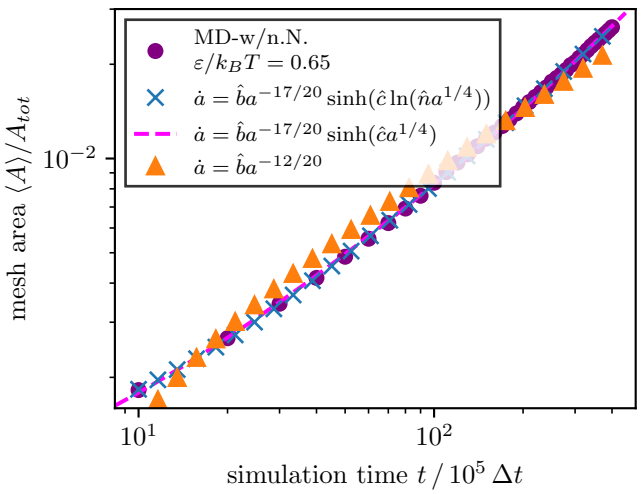

FIG. S34. Comparison of fits at different levels of simplification to MD-w/n.N. simulation data. The dashed line corresponds to the fit presented in the main text in Fig. 2f. The result obtained with the first approximation (dashed line) of $C \approx$ const is barely distinguishable from the scaling law relation without further simplification (crosses). The small force approximation (triangles) does not allow a good fit to the measured data.

small forces, that is for small arguments of the hyperbolic sine, $\sinh(x) \approx x$ can be linearized, and we obtain explicit power law solutions, $a(t) \sim t^{20/17}$ for MD-w/o n.N. and $a(t) \sim t^{20/32}$ for MD-w/n.N. and EC-LJ. We assess the quality of both approximations ($C =$ const and the linearization) by solving the differential equations numerically and fitting the parameters to the measured mean mesh areas as a function simulation time.

A comparison of the theory curves thus obtained for the different levels of approximation is shown in Fig. S34 taking the example of the MD-w/n.N. system. The result obtained with the assumption $C =$ const is virtually indistinguishable from the full theory confirming our conjecture based on the slow variations of C. The linearization of the hyperbolic sine function, however, gives a significantly worse description of the simulation data, indicating that the thermally activated motion observed in the simulations of bundles (see previous Sec. IX) is in fact relevant for the coarsening dynamics of the bundled networks. Furthermore, the sensitivity of the coarsening dynamics to details of the interactions (e.g. MD-w/o n.N. vs. MD-w/n.N.) seems to be due to the sliding velocity v, where the propagation of the thermally activated motion along the polymer is found to be very sensitive to the interactions (cf. $B \sim L_B^{-1.2}$ and $B \sim L_B^{-2.7}$ in Fig. S32).

Using the differential equations stated in (11), we obtain the graphs shown in Fig. 2f in the main text and equivalently Fig. S35.

The fit procedure suffers from the typical problem that the reference values a span more than one order of magnitude and deviations to measurements at early simulation times are virtually irrelevant in the least square optimization. To obtain a well-behaved fit over the entire range of simulation times, we introduced weights. Namely, the weight assigned to each mean value $a(t)$ is the number of meshes it represents. The fit parameters thus obtained are listed in the legends of Fig. S35. The fit procedure gives considerable uncertainties on the fit parameters which highlights our simplifications of the delicate microscopic sliding dynamics.

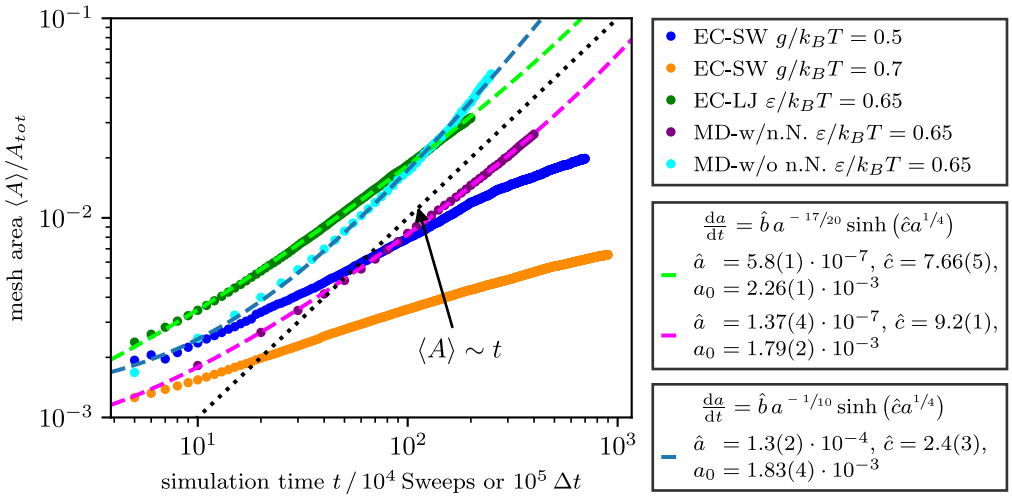

FIG. S35. Fit of the mean mesh area $a = \langle A\rangle/A_{tot}$ for different sets of simulations with the differential equations (11). The computed fit parameters are included in the legends, where $a_0 = a(t_0)$ denotes the initial value used in the numerical integration routine at the first analysed simulation snapshot. The dotted black line $\langle A\rangle \sim t$ serves as a guide to the eye.

XI. EXTENSION TO 3D SYSTEM

In this work, we focused on flat, quasi-2d geometries and applied hard wall boundary conditions in the z-direction where the system size is reduced $L_z \ll L_{x,y}$ to reduce the computational effort. In the cell, cytoskeletal networks will be three-dimensional and a natural and important extension of our work is to consider genuine 3d systems [6, 9, 12, 13, 23] with respect to foam-like properties or cellular structure laws. The simulation snapshots in Fig. S36 demonstrate that this is possible (with increased computational effort). We expect similar scaling laws regarding the network structure, because the 3d network structures also emerge from edge length minimization as in 2d.

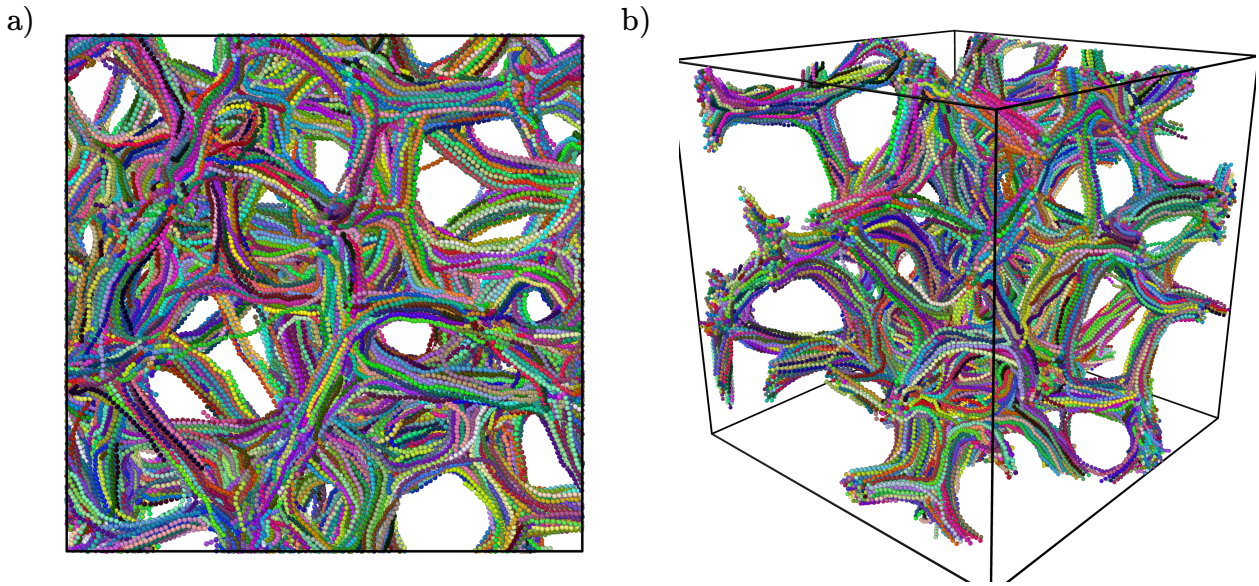

FIG. S36. Snapshot of a MD simulation of 1000 polymers in a volume of size $100 \times 100 \times 100\,\sigma^3$ with periodic boundary conditions. Both snapshots show the same system state after a simulation time $t = 2 \cdot 10^6\,\Delta t$ as a side-view (a) or mimicking the perspective from slightly above the simulation cell (b). The polymers are colored arbitrarily in an attempt to aid the visual representation of the emerging bundled structure similar to an open-cell foam.

[1] T. A. Kampmann, D. Müller, L. P. Weise, C. F. Vorsmann, and J. Kierfeld, Event-chain monte-carlo simulations of dense soft matter systems, Front. Phys. **9**, 635886 (2021).
[2] W. Krauth, Event-chain monte carlo: Foundations, applications, and prospects, Front. Phys. **9**, 663457 (2021).
[3] E. A. J. F. Peters and G. de With, Rejection-free monte carlo sampling for general potentials, Phys. Rev. E **85**, 026703 (2012).
[4] T. A. Kampmann, H.-H. Boltz, and J. Kierfeld, Monte carlo simulation of dense polymer melts using event chain algorithms, J. Chem. Phys. **143**, 044105 (2015).
[5] J. Kierfeld, T. Kühne, and R. Lipowsky, Discontinuous unbinding transitions of filament bundles, Phys. Rev. Lett. **95**, 038102 (2005).
[6] R. J. Pandolfi, L. Edwards, D. Johnston, P. Becich, and L. S. Hirst, Designing highly tunable semiflexible filament networks, Phys. Rev. E **89**, 062602 (2014).
[7] A. Sengab and R. Picu, Filamentary structures that self-organize due to adhesion, Phys. Rev. E **97**, 032506 (2018).
[8] R. Picu and A. Sengab, Structural evolution and stability of non-crosslinked fiber networks with inter-fiber adhesion, Soft Matter **14**, 2254 (2018).
[9] L. T. Nguyen, W. Yang, Q. Wang, and L. S. Hirst, Molecular dynamics simulation of f-actin reveals the role of cross-linkers in semi-flexible filament assembly, Soft Matter **5**, 2033 (2009).
[10] T. A. Kampmann, H.-H. Boltz, and J. Kierfeld, Controlling adsorption of semiflexible polymers on planar and curved substrates., J. Chem. Phys. **139**, 034903 (2013).
[11] S. Deshpande and T. Pfohl, Hierarchical self-assembly of actin in micro-confinements using microfluidics, Biomicrofluidics **6**, 034120 (2012).
[12] E. P. DeBenedictis, Y. Zhang, and S. Keten, Structure and mechanics of bundled semiflexible polymer networks, Macromolecules **53**, 6123 (2020).

[13] R. D. Groot, Mesoscale simulation of semiflexible chains. II. Evolution dynamics and stability of fiber bundle networks, J. Chem. Phys. **138**, 224904 (2013).
[14] H. Watanabe, N. Ito, and C.-K. Hu, Phase diagram and universality of the lennard-jones gas-liquid system, J. Chem. Phys. **136**, 204102 (2012).
[15] V. Popov and J. Gray, Prandtl-tomlinson model: History and applications in friction, plasticity, and nanotechnologies, J. Appl. Math. Mech. **92**, 683 (2012).
[16] A. Ward, F. Hilitski, W. Schwenger, D. Welch, A. W. C. Lau, V. Vitelli, L. Mahadevan, and Z. Dogic, Solid friction between soft filaments, Nat. Mater. **14**, 583 (2015).
[17] M. Illig, K. Jahnke, L. P. Weise, M. Scheffold, U. Mersdorf, H. Drechsler, Y. Zhang, S. Diez, J. Kierfeld, and K. Göpfrich, Triggered contraction of self-assembled micron-scale DNA nanotube rings, Nat. Commun. **15**, 2307 (2024).
[18] P. G. de Gennes, Reptation of a polymer chain in the presence of fixed obstacles, J. Chem. Phys. **55**, 572 (1971).
[19] The scaling observed in Fig. S30 can be approximately reproduced if we set the respective force $F = 0.5k_BT/\sigma$ or $F = 5k_BT/\sigma$ and fit a power law to $a(N_{marker})\sinh(b(N_{marker})F)$.
[20] We expect some deviations from the Frenkel-Kontorova model predictions because the model is a crude approximation of the marker polymer in the bundle, e.g. the potential due to the other polymers is not strictly periodic and the motion is not completely one-dimensional. Nonetheless, the bundle width is narrow compared to the bundle length and the applied force induces a preferential direction.
[21] O. M. Braun and Y. S. Kivshar, Nonlinear dynamics of the frenkel–kontorova model, Phys. Rep. **306**, 1 (1998).
[22] F.-J. Elmer, Avalanches in the weakly driven frenkel-kontorova model, Phys. Rev. E **50**, 4470 (1994).
[23] M. J. Stevens, Bundle binding in polyelectrolyte solutions, Phys. Rev. Lett. **82**, 101 (1999).